





Stellar initial mass function in the 100-pc solar neighbourhood

Yu-Ting Wang (王雨亭) ^{1,2}, Chao Liu (刘超) ^{1,2,3,4}  [★] Jiadong Li (李佳东) ⁵

¹Key Laboratory of Space Astronomy and Technology, National Astronomical Observatories, CAS, Beijing 100101, People's Republic of China

²University of Chinese Academy of Sciences, Beijing 100049, People's Republic of China

³Institute for Frontiers in Astronomy and Astrophysics, Beijing Normal University, Beijing 100875, People's Republic of China

⁴Zhejiang Lab, Hangzhou, Zhejiang 311121, People's Republic of China

⁵Max-Planck-Institute for Astronomy, Königstuhl 17, Heidelberg D-69117, Germany

Accepted XXX. Received YYY; in original form ZZZ

ABSTRACT

The stellar initial mass function (IMF) is one of the most important astrophysical distribution function, and is defined as the mass distribution for stars formed in a single star-formation event and when they just enter the main-sequence stage. The measurement of IMF is challenging even in the solar neighbourhood where IMF can be extracted by star-counting. This is because the definition of the IMF should be handled cautiously, and there are multiple corrections should be made from observation to a well-founded measurement. We present a new parametrisation of the stellar IMF in the 100-pc solar neighbourhood, leveraging the astrometric and photometric data from *Gaia* DR3: we model the colour-magnitude diagram of the field star population while accounting for observational uncertainties, Malmquist bias, Lutz-Kelker bias, the effect of varying mass-luminosity relation caused by mixture of different metallicity, and the effect of unresolved binaries. In particular, we synthesise the binaries with a process imitating the dynamical evolution observed in star clusters to model their present-day mass-ratio distribution. We derive a stellar IMF consistent with canonical IMFs but with significantly reduced uncertainties: $\alpha_1 = 0.81^{+0.06}_{-0.05}$, $\alpha_2 = 2.12^{+0.04}_{-0.04}$, and a break point at $m_{\text{break}} = 0.41^{+0.01}_{-0.01} M_{\odot}$. Our model also constrains the binary fraction to $\sim 25\%$ and the *Gaia* DR3 angular resolution to $1.31^{+0.24}_{-0.29}$ arcsec. We also provide the ξ -parameter for our IMF to be $0.5075^{+0.0112}_{-0.0051}$ for the users to compare our result with other work.

Key words: stars: luminosity function, mass function – (stars:) Hertzsprung–Russell and colour–magnitude – Galaxy: stellar content – (Galaxy:) solar neighbourhood – methods: statistical

1 INTRODUCTION

The stellar initial mass function (stellar IMF) is one of the most important astrophysical distribution function, and its basic definition is the mass spectrum for stars formed in a single star-formation event and when they just enter the main sequence stage. The measurement of the stellar IMF is a challenging topic since stellar masses cannot be measured directly, and it is actually an abstract mathematical definition and not able to be extracted from any individual stellar population (*the IMF Unmeasurability Theorem*, Kroupa et al. 2013). Therefore, it is vital to clarify the specific definition of IMF in every individual work based on different populations and systems, and comparison between differently-defined IMFs should be careful.

Apart from single population systems, there exist composite population systems in the universe, which are the mixture of multiple star-forming events, e.g. field stars in the solar neighbourhood. The IMFs for composite stellar systems are called composite IMF, which should be the integration of stellar IMFs through space and time. The

IMF for external galaxies are also composite IMF and referred to as galaxy-wide IMF (gwIMF) in Kroupa et al. (2024). Composite IMFs are unequal to stellar IMFs, though correlated.

The IMF plays a very important role in astronomical studies. First, it acts as a basic input, i.e. a mass sampling function, for simulations in astronomy (e.g. simulations for dynamical evolution of clusters, population synthesis for galaxies, etc. Wang et al. 2020; Vazdekis et al. 2015). Moreover, the IMF can serve as useful tool for the understanding of physical process of baryon cycle in the universe. Since direct mass measurement for stars is difficult and inefficient (via binary orbit movements and asteroseismology), it is an easier way for us to extract the knowledge about star formation and evolution through the IMF in a statistical perspective.

There are two key issues in the field of IMF. The first is the nature of the IMF, that is, why the IMF is in the form of power-law combined with several characteristic masses. The power-law form seems to point out a generally scale-free process in the star-forming event, while the emergence of characteristic masses (turning points/break points/peaks) in the middle of power-law might indicate additional physics that provide a termination scale for the cascade (Guszejnov et al. 2016) of star formation.

The second is the variation of the IMF (Kroupa et al. 2013). The-

[★] E-mail: liuchao@nao.cas.cn

ories of star formation predict that the IMF varies with the stellar environment (Bonnell et al. 2006; Clark et al. 2011). However, in early studies, star counts in star-resolving regions did not observe variations in the IMF over 3σ level (Bastian et al. 2010). As the quality of observational data improved, many studies reported evidence of IMF variations across different galactic environments recently. Since these studies focused on extragalactic systems, what they discovered are actually the variation of the gwIMFs. According to the IGIMF theory (Weidner & Kroupa 2005), the high-mass end of the gwIMF is varying with the average star formation rate (SFR) of galaxies even when setting the stellar IMF universal. This means that, in composite populations, the stellar IMF and star formation history (SFH) are highly degenerated at high-mass end ($m \gtrsim 1.0M_{\odot}$). Therefore, if we want to study the variation of stellar IMF in composite stellar systems, it is simpler to do it in the low-mass end ($m \lesssim 1.0M_{\odot}$) where stars hardly evolve during their life-time, and where the composite IMF is equally to stellar IMF.

As a prerequisite, it is essential to establish a method capable of accurately measuring the stellar IMF of field stars in the Milky Way (MW). Stellar samples from the solar neighbourhood are part of the field stars of the MW, and also are a golden sample for investigating the IMF of brown dwarfs and low-mass stars. In the solar neighbourhood, we can acquire the highest-quality photometric, trigonometric parallax, and spectroscopic measurements. Precise measurement and detailed analysis of the stellar IMF in the solar neighbourhood can serve as a bridge to regions such as the overall Milky Way, star-forming regions, the Galactic center, star clusters, and external galaxies.

In 1955, Salpeter published a seminal work on the IMF (Salpeter 1955), and he described the IMF using a single power-law distribution, expressed as

$$\frac{dN}{dm} = \xi(m) = km^{-\alpha}, \quad (1)$$

where dN represents the number of stars within the mass interval dm . He derived the mass distribution for main sequence stars ranging from 0.4 to $10 M_{\odot}$ in the vicinity of the sun by combining the largest observational samples of nearby stellar luminosity functions

$$\phi(M_V) = \frac{dN}{dM_V} \quad (2)$$

available at the time. This resulted in determining the slope of the mass distribution as $\alpha = 2.35$, a relation he termed the “original mass function” for stars. In Salpeter (1955), the single power-law IMF is referred to as the Salpeter IMF, and any IMF with a single power-law index α close to ~ 2.35 (or $\Gamma \sim 1.35$) is said to possess the “Salpeter slope”.

Subsequently, pencil-beam survey-technique was developed, focusing on small field of view ($< 5 \text{ deg}^2$), typically for extragalactic scientific purposes. Research on the IMF began to focus on two types of samples: nearby (5.2 pc) trigonometric parallax samples (Jahreiß & Wielen 1997) and deeper pencil-beam stellar count data (Gould et al. 1996; York et al. 2000a). Miller & Scalo (1979) calculated the IMF for stars with masses less than $1.0 M_{\odot}$ using nearby stellar samples, while Scalo (1986) primarily relied on more recent pencil-beam observational samples.

In the 1990s, due to the better understanding of the non-linearity in the stellar mass-luminosity relation (MLR) and a detailed analysis of the effects of unresolved binary systems (Kroupa 1992), the IMF for low-mass stars was revised. For the first time, the shape of the luminosity function was explained from the perspective of stellar physics, and all biases in stellar count data based on trigonometric parallax and photometric parallax were rigorously modelled. This addressed the

differences in results obtained by Miller & Scalo (1979) and Scalo (1986), which are, specifically, the disparities between luminosity functions and mass functions derived from the 5.2 pc trigonometric parallax sample and the photometric parallax samples from pencil-beam surveys directed towards the galactic poles. Ultimately, they presented the canonical “Kroupa IMF” which is characterized as a piece-wise power-law distribution:

$$\xi(m) = \begin{cases} m^{-1.3}, & 0.08 < m/M_{\odot} \leq 0.5 \\ m^{-2.3}, & 0.5 < m/M_{\odot} \leq 1.0 \\ m^{-2.7}, & m/M_{\odot} > 1.0 \end{cases} \quad (3)$$

Reid et al. (2002a) utilized updated trigonometric parallax data from the Hipparcos mission to confirm the results of Kroupa (1992). Chabrier (2003) refitted the mass function for the mass range of 0.07 to $1.0 M_{\odot}$ with a log-normal function for the lower mass end, while retaining the “Salpeter IMF” form for the higher mass end. This bimodal mass function, characterized by a log-normal distribution with a mean (μ) of 0.08 and a standard deviation (σ) of 0.68 at the lower mass end, and by the Salpeter form at the higher mass end, was subsequently termed the “Chabrier IMF”. Despite of the difference in mathematical forms, Chabrier IMF is statistically indistinguishable from the Kroupa IMF (Kroupa 1992).

In the 2000s, large-scale digital sky surveys such as the Two Micron All Sky Survey (2MASS; Skrutskie et al. 2006) and the Sloan Digital Sky Survey (SDSS; York et al. 2000b) emerged, which conducted more uniform and deeper photometric imaging across extensive areas of the sky. Covey et al. (2008) compiled photometric catalogs from SDSS, 2MASS, etc. to study the present-day mass function (PDMF) of field stars, comprising approximately 30,000 low-mass stars. Bochanski et al. (2010) employed a photometric sample from the Sloan Digital Sky Survey Data Release 6, covering 8400 deg^2 of the sky and comprising 15,000,000 stars, to derive photometric parallaxes and determine the luminosity function (LF) and mass function (MF) for low-mass stars in the range $0.1 \lesssim m/M_{\odot} \lesssim 0.8$, finding good consistency with previous work. Nonetheless, the computation of photometric parallaxes involves the use of colour-luminosity relations derived from limited spectroscopic observations, introducing multiple uncertainties.

The *Gaia* astrometric mission (Gaia Collaboration et al. 2018) has revolutionized the trigonometric parallax catalog of the Milky Way. With data from *Gaia* DR2, Sollima selected over 120,000 stars to study the IMF of the Galactic disc (Sollima 2019). His model accounted for unresolved binary systems, metallicity distribution, star formation history, and the variation in stellar number density across the galactic disc, along with all observational effects. His results are also consistent with the canonical IMF within margins of error. After this, Hallakoun & Maoz (2021) and Li et al. (2023) also used *Gaia* data to study the variation of IMF in the solar neighbourhood. However, few meticulous field-star population synthesis model was established with detailed binary modelling in the solar neighbourhood.

In this study, we intend to use the most up-to-date, largest, and the most complete sample with photometric and astrometric observation in the solar neighbourhood to remeasure the stellar IMF for the field stars in this region. In the model, the effects of Malmquist bias, Lutz-Kelker bias, the variation of mass-luminosity relation (MLR) for stars with different metallicity, and the effect of multiple systems will be handled comprehensively. In Sec.2 we describe the observational data, what cuts we have done, and how we check the quality and completeness of the data. In Sec.3 we present our analysis methods, including clarification of basic definitions, procedure of how we

synthesize the field star population, and how we use Bayesian inference to obtain the posterior distributions of the parameters that we care for the solar neighbourhood field stars. In Sec.4 we describe the basic results of our work. Furthermore, we investigate the reliability of the method through several tests, and listed some caveats in Sec.5, and finally present our conclusions in Sec.6.

2 DATA

2.1 *Gaia* Early Data Release 3: The *Gaia* Catalogue of Nearby Stars (GCNS)

In this work, we utilize the catalog that *Gaia* Early Data Release 3 (EDR3) provides which contains all the objects with reliable astrometry and non-zero probabilities of being within 100 pc from the sun, which will be referred to as the *Gaia* Catalogue of Nearby Stars (GCNS; [Gaia Collaboration et al. 2021b](#)) hereafter. The catalog includes over 330,000 objects in the 100-pc solar neighbourhood. We check the photometry, astrometry and completeness of sources the GCNS catalog before we get to detailed analysis of the initial mass function (IMF) embedded in the data.

For the G -, G_{BP} - and G_{RP} -band apparent magnitude provided in the catalog, three corrections/problems are taken into account ([Riello et al. 2021](#)):

First of all, there are systematics due to use of default colour in the Image Parameter Determination (IPD) process in calculating the G -band fluxes in *Gaia* EDR3. The effect has been corrected in the *Gaia* DR3 catalog, so we substitute the G -band magnitude with DR3 value .

Second, the mean G_{BP} flux for faint red sources is overestimated because they excluded epochs with a calibrated flux lower than $1 \text{ e}^- \text{ s}^{-1}$ when computing the weighted mean flux for a source. The operation is necessary because a source with a flux lower than this limit cannot be observed as a normal distribution. From the test carried out in [Riello et al. \(2021\)](#), stars with $G_{BP} < 20.3$ mag suffer little from this effect. Thus, we perform a cut on G_{BP} mag with $G_{BP} < 20.3$ mag.

Last, we consider the crowding effect. G_{BP} and G_{RP} fluxes are the integrated mean fluxes obtained from CCD windows of $3.5'' \times 2.1''$, whereas the G flux is determined from Point Spread Function (PSF) or Line Spread Function (LSF) fitting to an object window from the astrometric field CCDs ([Golovin et al. 2023](#)). In the crowded field, the sources measured in G_{BP} and G_{RP} -band tend to be brighter and bluer. These stars with problematic BP/RP photometry can be identified using the parameter β defined in Eq.1 using the columns from *Gaia* EDR3 archive. We remove this part of semi-resolved sources ($\beta < 0.5$) which only account for about 4 per cent of the whole data set which caused modest effect on completeness.

$$\beta = \frac{\text{phot_bp_n_blended_transits} + \text{phot_rp_n_blended_transits}}{\text{phot_bp_n_obs} + \text{phot_rp_n_obs}} \quad (4)$$

As for the astrometric information in the catalog, we consider zero-point correction and include the NSS parallax solution.

We intend to conduct parallax zero-point corrections using the official package `gaiadr3-zero-point` which can be applied on *Gaia* EDR3 and DR3 data ([Lindegren et al. 2021](#)). However, we find that the absolute change in parallax correcting our sample is less than 1 per cent. Given the small impact of the correction, and the fact that some of our sources lack parameters required by the zero-point

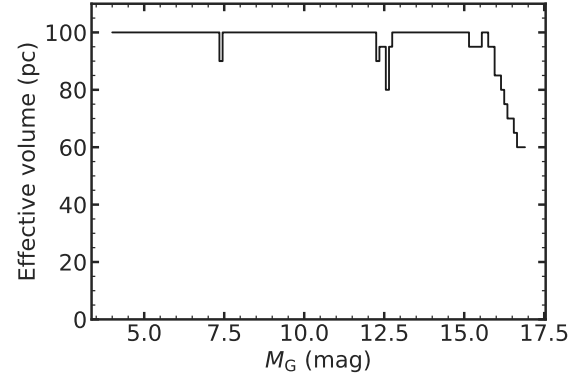


Figure 1. Completeness limit as a function of absolute magnitude in the G -band.

correction package and that completeness means more in the star counting approach to gain the IMF, we neglect the effect of zero-point correction. The zero-point correction should not be neglected when the sample covers wider distance range.

Furthermore, astrometric solution will obtain suspicious measurement on very nearby multiple systems since the internal orbital motion of the system can make it challenging to isolate their parallax motion accurately. So we make use of the non-single star (NSS) parallax solution to replace those suffered from this issue ([Gaia Collaboration et al. 2023b](#)).

2.2 Completeness test

The completeness of a volume-limited dataset, such as GCNS, is crucial for the derivation of the IMF. The selection effect primarily impacts the absolute magnitude M_G and position (e.g., Galactic latitude and Galactic longitude), while the colour $G_{BP} - G_{RP}$ remains relatively unaffected ([Cantat-Gaudin et al. 2023](#)). Since the distribution of stars of the catalog GCNS is relatively homogeneous, variations of selection effect on position can be ignored, we then examine the completeness at various M_G bins with V/V_{\max} technique ([Schmidt 1968; Felten 1976; Tinney et al. 1993](#)).

The stellar density distribution of the thin disk in our Milky Way can be described with exponential distribution $n(R_{xy}, z) \propto \exp\{-R_{xy}/h_R\} \cdot \exp\{-z/h_z\}$, where R_{xy} is the Galactocentric distance along the Galactic plane and z the height above the Galactic plane. We assess the completeness of our sample GCNS by the comparison to the exponential disk model above using Kolmogorov–Smirnov (K-S) test. We sample from the $n(R_{xy}, z)$ distribution to generate the control sample with expected density profile. Here h_{xy} and h_z are fixed to 3 kpc and 300 pc, respectively ([Vogel 2017](#)). The spatial position of the sun is set to $(X_\odot, Y_\odot, Z_\odot) = (-8.35, 0, 0.01)$ kpc ([Griv et al. 2021](#)). This can lead to the expected number distribution of stars for our control sample along the distance from the sun $n_{\text{ctrl}}(d)$. While we assume an exponential disk model, substructures within 100 pc (e.g., stellar streams) could introduce minor deviations, though their impact is likely negligible given the homogeneity observed in *Gaia* data ([Gaia Collaboration et al. 2021b](#)).

Adopting the similar method in [Golovin et al. \(2023\)](#), we conduct the K-S test in sliding bins of M_G with 0.1 mag step and 1 mag bin width, favouring robustness and resolution. We perform the test to decide whether the number distribution along the distance from the sun of the GCNS data ($n_{\text{GCNS}}(d)$) is compatible with that of our

control sample ($n_{\text{ctrl}}(d)$). In an individual M_G bin, the test can be done in different distance range, and this can give us the “complete volume” in the M_G bin, which is shown by effective volume (pc) from the sun in Fig. 1. More detailed description of the effective volume calculation is written in Appendix A. Fig. 1 shows that, except for the natural decrease of completeness volume for dimmer stars with $M_G > 15$ mag caused by astrometric quality requirements of GCNS, stars are volume-completed in the 100-pc solar neighbourhood. Therefore, no additional selection effect correction is needed in our approach to the intrinsic luminosity function in the M_G range from 4.1 to 12.1 mag.

2.3 Sample selection

Next we will explain how we select the stars in the catalog of GCNS for the calculation of our IMF. In Fig. 2, we show the colour-magnitude diagram (CMD) for all stars in GCNS with gray dots. We compute the absolute magnitude with the equation

$$M_G = G + 5\log_{10}(\varpi) - 10, \quad (5)$$

where M_G stands for the absolute magnitude of *Gaia* G-band, G the G-band apparent magnitude, and ϖ the parallax measured by *Gaia*.

In this study, we focus on the initial mass function (IMF) of low-mass main-sequence stars ($0.15 < m/M_\odot < 1.0$), which experience minimal evolutionary effects, simplifying our modelling approach. Interstellar extinction is negligible within the 100-pc solar neighbourhood (Edenhofer et al. 2024), allowing us to rely on *Gaia* DR3 photometry without correction. To select main-sequence stars, we adopt the boundary from Penoyre et al. (2022), defined as $M_G - 3.2(G_{\text{BP}} - G_{\text{RP}}) < 3.8$. For the low-mass end, we use PARSEC iso-mass lines at $0.15 M_\odot$ and apply a filter of $M_G < 12.1$ mag to ensure model accuracy. At the high-mass end, a horizontal cut at a fixed M_G would include metal-rich stars above $1.0 M_\odot$, which undergo significant evolution. Instead, we use the iso-mass line for unevolved $1.0 M_\odot$ stars, shown as the upper black dotted line in Fig. 2. The resulting sample, colour-coded by density in Fig. 2, comprises 233,217 stars for further analysis.

3 METHOD

3.1 General description

We develop a population synthesis model to reproduce the observational properties of field stars within the 100-pc solar vicinity, starting from an stellar initial mass function (stellar IMF). In this section, we first clarify key definitions, including the stellar IMF and binary fraction. We then identify critical corrections for observational biases and physical effects. Finally, we describe the equal-frequency binning strategy used throughout our analysis to minimize statistical biases.

To extract the initial mass function from the field stars, there are some definitions that should be clarified. First, the IMF that we pursue in this article is the stellar IMF. The stellar IMF represents the initial mass distribution of a single star-formation event and is the distribution of all stars (not systems) in the event, thereby counting all individual components in multiple systems (Kroupa et al. 2013). Second, the term “binary fraction” refers to the proportion of binary systems (including resolved and unresolved ones) relative to the total number of stellar systems. Specifically, when calculating this fraction, each binary star system is treated as a single unit, regardless of the number of stars it contains.

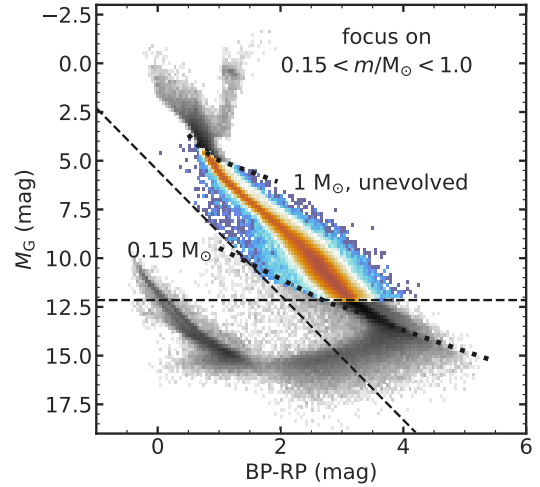


Figure 2. colour-magnitude diagram for stars in the 100-pc solar neighbourhood. The scatter with gray colour map illustrates the density distribution for all GCNS sample, overlapped with the object density distribution resulting from our sample selection procedure in Sec. 2.3. Black dashed lines denote the selection standards for Main-sequence stars in Penoyre et al. (2022), while black dotted lines denote the iso-mass lines for $0.15 M_\odot$ and unevolved $1.0 M_\odot$ stars from PARSEC model.

We aim to reassess the IMF in the low-mass regime ($0.15 < m/M_\odot < 1.0$) using the field star sample from the 100-pc solar neighbourhood. Direct star counting and luminosity-to-mass conversion using a single mass-luminosity relation (MLR) curve is not feasible due to several potential issues: (1) sample completeness; (2) Lutz-Kelker bias; (3) stellar evolution; (4) unresolved multiple systems; and (5) variations in the stellar mass-luminosity relation (MLR) due to chemical composition, age, and spin (as concluded by Kroupa et al. 2013).

In this study, we disregard the effects of stellar spin and age distribution, as they have negligible impact on the low-mass IMF ($0.15 < m/M_\odot < 1.0$). For low-mass stars ($< 1 M_\odot$), rotation plays a minimal role in their position on the colour-magnitude diagram (CMD), as these stars are not expected to be rapid rotators (Bastian & de Mink 2009). Regarding stellar evolution, assuming a constant star formation history and solar metallicity, PARSEC 1.2s stellar tracks (Bressan et al. 2012; Chen et al. 2014, 2015; Tang et al. 2014; Marigo et al. 2017; Pastorelli et al. 2019, 2020) indicate that for stars with masses $0.15 < m/M_\odot < 1.0$, only about 5 per cent are at the pre-main sequence stage, with virtually none above the turn-off point. By excluding evolutionary effects, we avoid making additional assumptions about the star formation history (SFH) of field stars. Consequently, our method focuses on correcting biases from: (1) sample completeness; (2) Lutz-Kelker bias; (3) unresolved multiple systems; and (4) variations in the stellar mass-luminosity relation (MLR) due to metallicity.

We have described the test on the sample completeness by V/V_{max} technique in Sec. 2.1, revealing that our sample is volume-completed in the mass range that we focus on. The Lutz-Kelker bias is a systematic bias meaning that, on average, the observed trigonometric parallaxes are larger than the true trigonometric parallaxes (Lutz & Kelker 1973). Thus, absolute magnitudes obtained from trigonometric parallaxes can also be biased. And the extent of this bias depends on the relative error, σ_ϖ/ϖ . According to Lutz & Kelker (1973), when σ_ϖ/ϖ increase from 0.025 to 0.175, the correction $< \Delta M >$ goes up from -0.01 to -0.43. There’s only $\sim 1\%$ of our

sample possessing $\sigma_{\varpi}/\varpi > 0.05$, so the correction is insignificant. Consequently, we need only consider the influence of stellar mass-luminosity relation (MLR) varying with metallicity and unresolved multiple systems in our model afterwards.

MLR varying with metallicity: The position of a star on the CMD (i.e., colour-magnitude diagram) can be determined by its mass, age, and metallicity. Generally, these three parameters are degenerated at some point, hence we cannot estimate stellar mass (also age, and metallicity) based solely on luminosity and colour. Fortunately, main-sequence stars on the CMD only slightly move with age, and their positions are largely determined by their masses, and their metallicities. Here, we plan to derive a metallicity distribution first based on *Gaia* XP spectra metallicity measurement (Li et al. 2023) and we will sample the metallicity for our model star according to this distribution in the forward modeling.

Unresolved multiple systems: We only consider the binaries instead of other multiple systems in the field population as other multiple systems only make up for $\sim 10\%$ of all systems for solar-type stars according to Moe & Di Stefano (2017).

The most straightforward way to model unresolved binaries is to pair two groups of stars drawing from the same IMF randomly, then synthesize the luminosity for the unresolved ones to match the observation. However, the mass-ratio distribution obtained by random pairing cannot match the observed ones (e.g. large sample wide binary statistics produced by Raghavan et al. 2010; El-Badry et al. 2019).

Specifically, the overall shape of the observed mass-ratio distribution (slopes, break point, etc.) is very different and a feature of the present-day mass-ratio distribution called twin phenomenon is identified, which is a statistical excess of nearly equal-mass binaries ($0.95 < q < 1$). The discrepancy will lead to ill-describing of the binary main sequence in our forward model. Thus, we introduce a procedure to modulate the random-pairing-like mass-ratio distribution to the observed one. The most intuitive way is to mimic the dynamical process of binary systems in star clusters to conduct the conversion. And dynamical evolution mainly works as the function of the binding energy of the binary system. Disrupted binaries will enter the field as single stars, thus affecting the shape of the observed mass function. However, the mass-ratio distribution has been suggested to be insensitive to dynamical evolution on the energy after formation (Parker & Reggiani 2013), so we build a dynamical operator as a function of both binding energy and mass ratio which will be described in detail in Sec. 3.2.

Important feature of our population synthesis model: We describe the binary population in the field with care, especially in the dimensions of their proportion and their mass-ratio distribution. We make a primary assumption about our dynamical evolution model that the stars in the solar neighbourhood were born in clusters, then most clusters got disrupted and their members mixed together to become field stars (Kroupa 1995a). This mixing process especially refers to the mixing of stellar density, metallicity, fractions of binary systems, and binary orbital parameter distributions (period distribution, mass-ratio distribution, etc.) Therefore, what we deduce is the parameters of a typical star cluster whose properties after dynamical evolution can describe the nowadays properties of field stars in the solar neighbourhood.

Binning strategy: For all binning operations in this article, we adopt the equal-frequency binning strategy proposed by Maíz Apellániz & Úbeda (2005), which minimizes the bias caused by unbalanced Poisson error in each bin.

3.2 Procedure

We use the population synthesis method to generate the synthesized CMD for the field stars in the 100-pc solar neighbourhood and constrain the IMF and binarity. In this population synthesis, we include new elements that we call “cluster-mode” dynamical evolution of binary orbit parameter distributions to fit for binary properties in the solar neighbourhood.

In general, we assume that stars form in clusters with 100% binaries, and both components in a binary system are sampled from the same IMF and are paired randomly at birth. Then the stars go through cluster-mode dynamical evolution and some binary systems disrupt, modifying the binary period and mass-ratio distribution to the present-day forms. And due to the angular resolution of *Gaia*, some of the survived binary systems cannot be resolved. Their observed luminosity and colour will shift with respect to those of the primary stars (the heavier component). Thus, we will decide which systems cannot be resolved and calculate their shifted luminosity and colour, which will then constitute the binary main sequence. At last, we can compare the synthesized present-day CMD and the observed one to constrain the IMF and binary properties.

We adopt the following procedure specifically to generate one set of model particles:

1. Birth distribution

(i). *Initial mass function (IMF):* we choose the functional forms for initial mass function to be piece-wise power-law as Kroupa’s in this work (Kroupa 1992). The parameters are α_1 , α_2 , m_{break} to represent the power-law indices and the position of the break point as in Eq. 6. We sample from the function for given parameters to be the mass collection of our model stars.

$$\xi(m) = \begin{cases} C_1 \cdot m^{-\alpha_1}, & m < m_{\text{break}}, \\ C_2 \cdot m^{-\alpha_2}, & m \geq m_{\text{break}} \end{cases} \quad (6)$$

(ii). *Metallicity distribution:* we sample from Johnson’s SU distribution (Johnson 1949) with $\gamma = 0.91^{+0.06}_{-0.05}$, $\delta = 1.61^{+0.05}_{-0.05}$, $\text{loc} = 0.10^{+0.01}_{-0.01}$ and $\text{scale} = 0.26^{+0.01}_{-0.01}$ to get the metallicity for every system. The derivation of these parameters is described in Appendix B. Since our dynamical evolution does not act on metallicity, it is reasonable not to distinguish birth metallicity distribution from present-day one.

(iii). *Birth binary population:* we assume that the binary fraction is 100 per cent at birth (Kroupa 1995a). We sample two groups of masses from the initial mass function, and matched them together to form the binary systems. In this way, the masses are paired randomly, meaning that the two component masses are uncorrelated when they are born, which is for simplicity and isn’t the case in reality. Noted that the range in which we sample the mass should be wider than we need when conducting the random-pairing, so we choose to sample from $0.09 M_{\odot}$ to $2.0 M_{\odot}$.

(iv). *Birth period distribution:* we adopt the birth period distribution obtained by Kroupa (1995a) for each binary system.

$$\Phi_{\log_{10} P}^{\text{birth}}(m_1 \lesssim 2.0 M_{\odot}) = 2.5 \frac{\log_{10} P - 1}{45 + (\log_{10} P - 1)^2} \quad (7)$$

(v). *Distance distribution:* we assume that the stellar volume density in the solar neighbourhood is constant, which means that the number of stars as a function of distance is $\rho(d) \sim d^2$. So we sample from this function to assign a distance to each system.

(vi). *Projected separations:* With period and mass for each component in a system, we can calculate the physical separation a_{phy} of

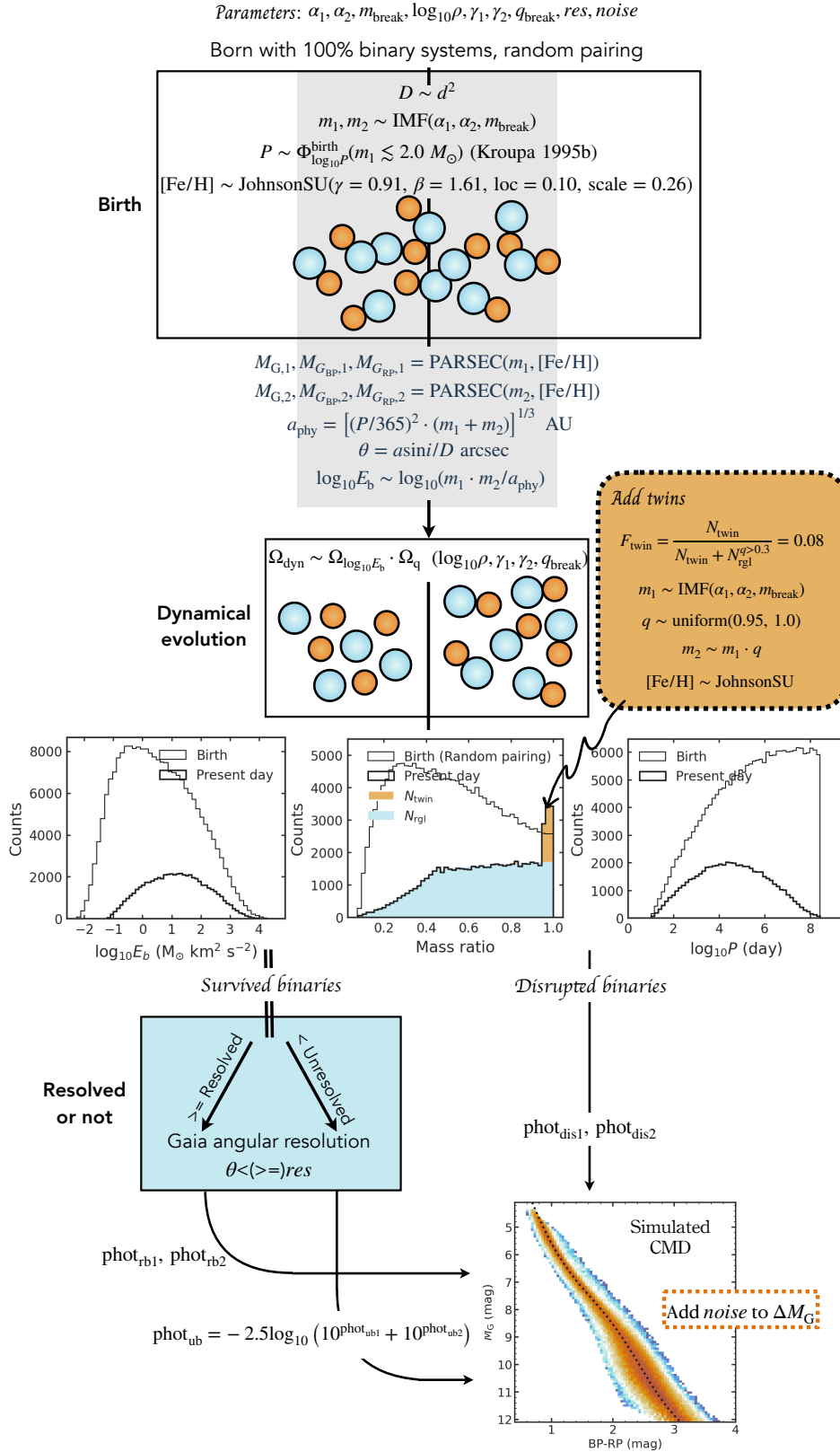


Figure 3. Flow chart for our population synthesis process. We assume that stars form in clusters with 100% binaries, and both components in a binary system are sampled from the same IMF and are paired randomly at birth, as described in the uppermost plot of this chart. Then the stars go through cluster-like dynamical evolution and some binary systems disrupt (phot_{dis}), modifying the binary period and mass-ratio distribution to the present-day forms. After this, we determine whether the survived binaries can be resolved by *Gaia* DR3 (survived, resolved ones, phot_{rb}). For those survived, unresolved binary systems (phot_{ub}), their photometry should be re-calculated.

Table 1. Notation Explanation

Symbols	Descriptions	Units
D	the distance of a system to the Sun;	pc
m_1, m_2	the mass of the primary star and the mass of the secondary star in a binary system;	M_\odot
P	the orbital period of a binary system;	day
$[\text{Fe}/\text{H}]$	the metallicity of a star;	dex
$M_{\text{G},1}, M_{\text{GBP},1}, M_{\text{GRP},1}$ $M_{\text{G},2}, M_{\text{GBP},2}, M_{\text{GRP},2}$	G, BP, RP-band absolute magnitude for the primary and secondary star respectively in a binary system;	mag
a_{phy}	the physical separation for the stars in a binary system;	AU
θ	the projected angular distance for the stars in a binary system;	arcsec
$\log_{10} E_{\text{b}}$	the binding energy of a binary system;	$M_\odot \text{ km}^2 \text{ s}^{-2}$
q	the mass ratio of a binary system, which is the mass of the secondary star divided by the mass of the primary star;	/
$\text{phot}_{\text{dis}1}, \text{phot}_{\text{dis}2}$		
$\text{phot}_{\text{rb}1}, \text{phot}_{\text{rb}2}$	the photometry ($M_{\text{G}}, M_{\text{GBP}}, M_{\text{GRP}}$) of disrupted, resolved and unresolved binary systems;	mag
phot_{ub}		
$\alpha_1, \alpha_2, m_{\text{break}}$	the parameters of our IMF, which is described with a piece-wise power-law distribution;	/
$\gamma, \beta, \text{loc}, \text{scale}$	the parameters of the metallicity distribution in the solar neighbourhood, which is described with a Johnson's SU distribution;	/
$\log_{10} \rho$	the characteristic density of the cluster in our dynamical evolution operator;	$M_\odot \text{ pc}^{-3}$
$\gamma_1, \gamma_2, q_{\text{break}}$	the parameters of our fitted present-day mass-ratio distribution, which is described with a piece-wise power-law distribution;	/
F_{twin}	the fraction of additionally added twin binaries, which is defined as in Eq.16;	/
$N_{\text{twin}}, N_{\text{rgl}}$	the number of twin binaries, and the number of “regular” binaries that go through the dynamical evolution;	/
res	the average angular resolution of <i>Gaia</i> DR3 on the stars in the 100-pc solar neighbourhood;	arcsec
$noise$	the standard deviation of the Gaussian noise added to our simulated ΔM_{G} distribution.	mag

the binary in the unit of AU by Kepler's Third Law. We then adopt a random binary orientation in the inference to get the projected separation a_{proj} . And we simply assume that binaries orbit in circular motion, so the projected distance a_{proj} will be $a \times \sin i$, where i is the inclination of the orbit plane. The system's observed angular distance is consequently

$$\theta = \frac{a_{\text{proj}}}{d} \quad (8)$$

II. Resolved or unresolved binary systems

We determine whether a systems is resolved by comparing the angular resolution of *Gaia* and the projected angular distance of the system. According to [Gaia Collaboration et al. \(2021a\)](#), the incompleteness in close pairs of stars starts below about 1.5 arcsec, which can be regarded as effective angular resolution of *Gaia* EDR3. This value will change for different regions in the sky, so we turn it into a parameter as well in our model as res . The systems with projected angular distances greater than res are considered resolved binary, while the others are unresolved binary. We need to synthesize the luminosity and colour of the two components for the unresolved systems.

III. Binary orbit evolution: from birth distribution to present-day distribution

(i). *Cluster-mode dynamical evolution operator*: evolution of binary period and binding energy distributions

In this paper, we will refer to the approach used by [Kroupa \(1995a\)](#) to describe the dynamical evolution of binary orbital parameters in the solar neighbourhood within a characteristic stellar cluster, known as a dominant mode cluster. The dynamical evolution of binaries in the cluster primarily acts on their binding energy, which is defined as Eq.5.

$$E_{\text{b}} = -G \frac{m_1 m_2}{2a} \quad (9)$$

G is the gravitational constant, m_1 and m_2 refer to the component masses, and a is the physical separation of the system.

Based on Kepler's Third Law, we can convert the right hand side of the equation Eq.5 to an equation relating to our sampling parameters in I.

$$\epsilon = (2\pi G)^{2/3} m_{\text{pr}}^{2/3} P^{-2/3} \frac{q}{(1+q)^{1/3}} \quad (10)$$

where m_{pr} is the mass of the primary star (heavier one), P is the period, and q is the mass ratio of the system.

This paper focuses solely on the process of binary dissolution during dynamical evolution. [Marks et al. \(2011\)](#), based on N-body

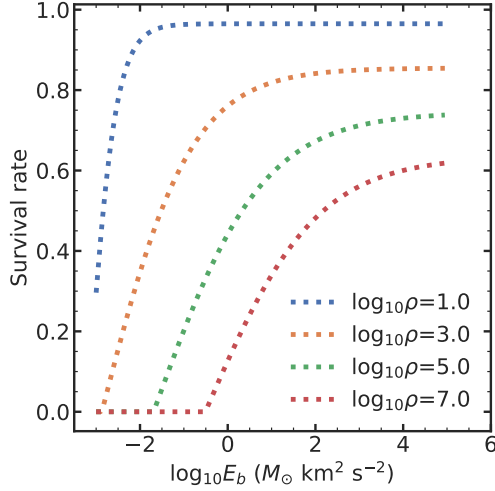


Figure 4. Dynamical evolution operator from Marks et al. (2011). The function reflects the survival rate of binary systems under certain binding energy in the dynamical evolution. The plot shows the variation of the functional form when different characteristic cluster densities $\log_{10}\rho$ are set up.

simulations, appears to be very helpful since they provided empirical relationships for the distribution of binary orbital parameters. Specifically, they derived the survival probabilities of binary systems at different evolutionary times and at different binding energies for a given set of cluster parameters, primarily the average density of the cluster (denoted as the parameter $\log_{10}\rho$ afterwards).

$$\Omega_{\log_{10}E_b}(\epsilon, t) = \begin{cases} \frac{\mathcal{A}}{1 + \exp[S(\epsilon - \epsilon_{\text{cut}})]} - \frac{\mathcal{A}}{2} & \epsilon \geq \epsilon_{\text{cut}} \\ 0 & \text{otherwise} \end{cases} \quad (11)$$

where ϵ represents the binding energy of the system, while \mathcal{A} , S and ϵ_{cut} are parameters that are functions of time t and the characteristic density of the stellar cluster $\log_{10}\rho$. Visualized form of this function can be seen in Fig.4.

According to Marks et al. (2011), the evolution of binary orbital parameter distribution during the dynamical evolution of star clusters ceases after approximately 5 million years (Myr) of formation. Therefore, in our model, we only apply the dynamical evolution operator at $t = 5$ Myr, see Eq.8. The remaining parameters that characterize the density of the star cluster, denoted as $\log_{10}\rho$, are treated as fitting parameters in our model. The information on the observed present-day binary fraction in the data can constrain $\log_{10}\rho$, as a higher characteristic cluster density implies a larger number of disrupted binaries, leading to a smaller binary fraction at present.

$$\epsilon_{\text{cut}} = \begin{cases} -4.40 + 0.54 \cdot \log_{10}\rho & \text{if result} > 3.2 \\ -3.2 & \text{otherwise} \end{cases} \quad (12)$$

$$\mathcal{A} = \begin{cases} 1.97 - 0.10 \cdot \log_{10}\rho & \text{if result} \leq 2 \\ 2 & \text{otherwise} \end{cases} \quad (13)$$

$$S = -\frac{1}{\exp[1.47 \cdot (\log_{10}\rho - 1.35)]} - 0.82, \quad (14)$$

when $t = 5$ Myr in Marks et al (2011).

The rightmost one of the middle plots in Fig.3 illustrate the changes

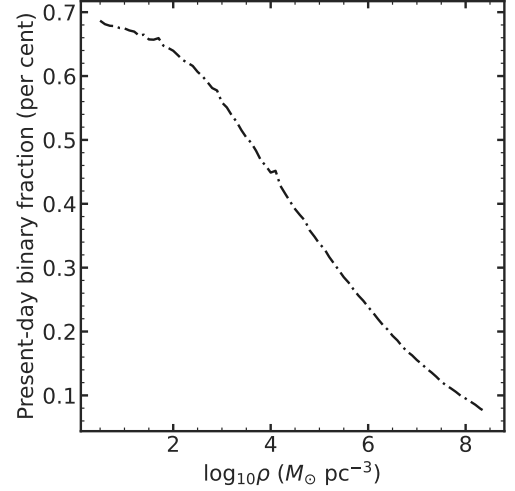


Figure 5. Relation of the characteristic cluster density in our dynamical evolution operator and subsequent present-day binary fraction.

in the distribution of binary periods after the application of the dynamical evolution operator under certain parameter settings. We find that when we only apply Eq.11 to the binary population, the period distribution is significantly altered, while the mass-ratio distribution remains unchanged. This finding is consistent with the statement made by Parker & Reggiani (2013) that the distribution of mass ratios is insensitive to dynamical evolution. It suggests that binaries with the same mass ratio experience similar dissolution rates during this process.

(ii). Mass-ratio distribution evolution operator

To achieve the transformation of the mass-ratio distribution from a random-pairing form to the present-day distribution, which can be constrained using observational data, we describe the present-day mass-ratio distribution using two power-law segments and a break point. The parameters involved are denoted as γ_1 , γ_2 , and q_{break} . The random-pairing mass-ratio distribution is dependent only on the form of the IMF. Hence, we can derive an evolution operator for the mass ratio, denoted as Ω_q , by dividing the present-day mass-ratio distribution by the mass-ratio distribution obtained from random pairing with a given IMF. The overall expression of the operator can be written as follows:

$$\Omega = C \cdot \Omega_{\log_{10}E_b} \cdot \Omega_q \quad (15)$$

The operator is normalized by C to ensure that the overall dissolution rate of the binary systems remains the same as when only the dynamical evolution operator $\Omega_{\log_{10}E_b}$ is applied.

IV. Twin binaries

In the history of multiple system studies, plenty of work has reported the discovery of a puzzling feature called twin phenomenon (Raghavan et al. 2010; Duchêne & Kraus 2013; Moe & Di Stefano 2017; El-Badry et al. 2019), which can also be located in our wide binary mass-ratio distribution at $q = 0.95 - 1.0$ in Fig.C1 with $F_{\text{twin}} = 0.08$. El-Badry et al. (2019) suggests that twins are likely form from a mechanism different from other binaries, e.g., competitive accretion from a circumbinary disc. In this way, the accretion rate from a circumbinary disc is usually higher for the secondary than the primary (sweeps out a larger radius in the disc), leading to nearly

equal masses of both stars. Thus, it is reasonable to add twin binaries to our synthesis model additionally without joining the dynamical process.

When regular binaries (form from non-twin mechanism) finish their dynamical process, we can then calculate how many twins should we add to our model, since our definition of F_{twin} is

$$F_{\text{twin}} = \frac{N_{\text{twin}}}{N_{\text{twin}} + N_{\text{rgl}}^{q>0.3}} \quad (16)$$

where $N_{\text{rgl}}^{q>0.3}$ means binaries forming in regular process with mass ratio larger than 0.3. In our model, *regular process* means that they are sampled from the IMF and randomly paired at birth, and then go through our dynamical evolution operator. This definition is the same as Moe & Di Stefano (2017) and El-Badry et al. (2019).

There will be resolved and unresolved twins as well, and we need their present-day period distribution to realize the process in our model. Here we simply assume that twins share the same period distribution as regular binaries. Therefore, we respectively calculate the number of resolved and unresolved twin binary systems $N_{\text{twin,rb}}$, $N_{\text{twin,ub}}$ with Eq. 16 by substituting $N_{\text{rgl}}^{q>0.3}$ with $N_{\text{rgl,rb}}^{q>0.3}$ and $N_{\text{rgl,ub}}^{q>0.3}$.

With the number of resolved and unresolved twins, we can then sample their mass ratio as uniform distribution from 0.95 to 1.0, and sample the masses of the primary with the IMF defined in Eq. 6. The masses of secondaries are therefore available. We apply the same metallicity distribution as regular binaries to these twins. And through PARSEC model, the photometry of each model star can be acquired interpolating on the grid of mass and metallicity. For unresolved twins, we should synthesize the photometry of two components.

V. Output of the model

For all resolved binary systems obtained from the aforementioned procedure, as well as unresolved but disrupted binary systems, we directly utilize the PARSEC model version 1.2s to obtain corresponding values of M_G , M_{GBP} , and M_{GRP} through interpolation of sampled masses and metallicities. For unresolved yet surviving binary systems, we synthesize the system's luminosity and magnitude (via flux) after obtaining the brightness and colours of individual stars. We employ the PARSEC model with initial masses $M_{\text{ini}} < 1 M_{\odot}$, metallicities $-1.0 < [\text{M}/\text{H}] < 0.6$, and age $\log_{10} \text{Age} = 9.5$.

Finally, we obtain a set of model stars that incorporate the effects of unresolved binary systems. To mitigate the inaccuracies of stellar models at the low-mass end (Chen et al. 2014), we separately fit the ridge lines $(\text{BPRP} - M_G)_{\text{c,mod}}$ and $(\text{BPRP} - M_G)_{\text{c,obs}}$ for the simulated CMD and the observed CMD, respectively, and subtract the ridge lines from the CMDs to get ΔM_G . After this, we consider the observational uncertainty by adding a Gaussian noise model to the simulated ΔM_G , where the means are set to the original simulated ΔM_G value, and the variation *noise* is assumed to be universal and set as a free parameter in our model. The observational uncertainty of M_G is insignificant relative to the span of the luminosity function.

Subsequently, by comparing the distributions of M_G and the noised residual distribution ΔM_G after subtracting the ridge line, we can constrain the parameters $\alpha_1, \alpha_2, m_{\text{break}}$ (IMF), $\gamma_1, \gamma_2, q_{\text{break}}$ (mass-ratio distribution), *res* (average resolution of *Gaia*), $\log_{10} \rho$ (cluster-mode dynamical evolution), and *noise*. The whole process is depicted in the flowchart Fig. 3.

VI. Bayesian estimation of the best parameters

We establish the likelihood function on the distribution of M_G (i.e. the luminosity function) and the distribution of ΔM_G separately. The ΔM_G is defined as

$$\Delta M_G = M_G - M_{\text{G,ridge}}(G_{\text{BP}} - G_{\text{RP}}) \quad (17)$$

which means the variation of M_G relation to the ridge line of the CMD. The information of binary fraction and mass-ratio can be represented better in ΔM_G distribution, while the information of stellar mass distribution in M_G distribution.

The observational and model M_G and ΔM_G data are binned in the same equal-binning strategy and the distributions can be denoted as $\{\phi_{\text{obs},i}\}$, $\{\phi_{\text{mod},i}\}$ and $\{\psi_{\text{obs},i}\}$, $\{\psi_{\text{mod},i}\}$, respectively. The likelihood function for one bin can be depicted as Gaussian distribution considering the observational uncertainties and Poisson error. The likelihood function and posterior are written in Eq. 18 and Eq. 19.

$$\begin{aligned} \mathcal{L}_i = & -\frac{1}{\sqrt{2\pi(\sigma_{\text{obs},i}^2 + \sigma_{\text{Poi},\phi_i}^2)}} \exp \left\{ -\frac{(\phi_{\text{obs},i} - \phi_{\text{mod},i})^2}{2(\sigma_{\text{obs},i}^2 + \sigma_{\text{Poi},\phi_i}^2)} \right\} \\ & -\frac{1}{\sqrt{2\pi(\sigma_{\text{obs},i}^2 + \sigma_{\text{Poi},\psi_i}^2)}} \exp \left\{ -\frac{(\psi_{\text{obs},i} - \psi_{\text{mod},i})^2}{2(\sigma_{\text{obs},i}^2 + \sigma_{\text{Poi},\psi_i}^2)} \right\} \end{aligned} \quad (18)$$

$$\begin{aligned} P(\alpha_1, \alpha_2, m_{\text{break}}, \gamma_1, \gamma_2, q_{\text{break}}, \log_{10} \rho, \text{res} \mid \{\phi_{\text{obs},i}\}, \{\psi_{\text{obs},i}\}) \\ = \text{prior}(\alpha_1, \alpha_2, m_{\text{break}}, \gamma_1, \gamma_2, q_{\text{break}}, \log_{10} \rho, \text{res}) \cdot \prod_i \mathcal{L}_i \end{aligned} \quad (19)$$

3.3 Sample from the posterior

We have a high-dimensional posterior depicting the joint probability distribution of $\alpha_1, \alpha_2, m_{\text{break}}, \gamma_1, \gamma_2, q_{\text{break}}, \log_{10} \rho$, and *res*. For a global view of the posterior distribution, we first draw a rough 8-dimension grid for the posterior to inspect the values of the parameters where the maximum posterior lies. Through this process, we find that the parameters of the mass-ratio distribution cannot be constrained well, which we will further discuss in Sec. 5.1. Therefore, we give a very sharp Gaussian prior for $\gamma_1 \sim \mathcal{N}(1.89, 0.23^2)$, $\gamma_2 \sim \mathcal{N}(0.20, 0.13^2)$ and $q_{\text{break}} \sim \mathcal{N}(0.44, 0.02^2)$ by the knowledge that we obtain from wide binaries, see Appendix C for detailed calculation. Additionally, we add the prior for the binary fraction according to Moe & Di Stefano (2017) to be $\sim \mathcal{N}(0.4, 0.05^2)$.

When running the MCMC program, we find that the randomness caused by sampling potentially leads to multi-modal posterior distribution. This feature makes emcee very hard to accomplish its required auto-correlation time and reach the point of convergence. Hence, we set the stretch scale parameter in emcee $a = 1.0$ to increase the step size to prevent the walker from being stuck in local minimum. And we combine the moves.DEMove and moves.DESnookerMove as recommended by the package contributor, which is also helpful in multi-modal situations (Foreman-Mackey et al. 2013b). We run the MCMC with 128 chains and 5,000 steps for each chain, and the final result is plotted in Fig. 7 in which the posterior distributions have been smoothed.

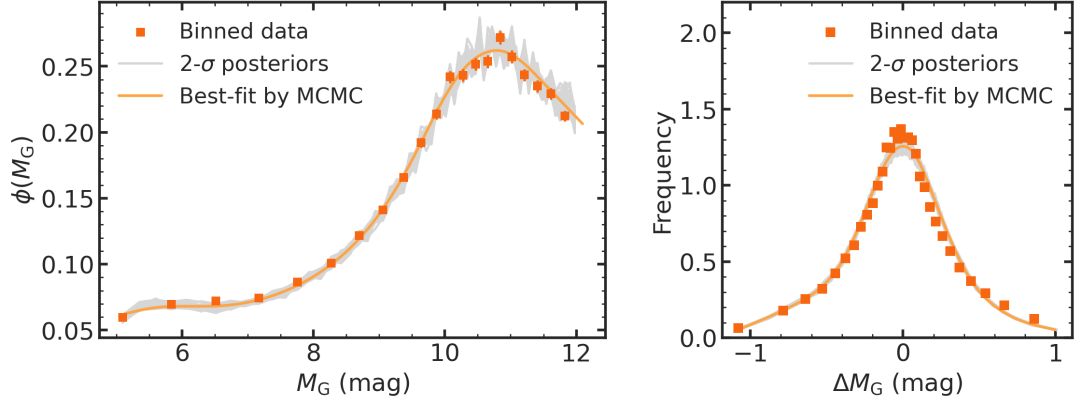


Figure 6. Comparison between observed luminosity function $\phi_{\text{obs}}(M_G)$, $\Delta M_{G,\text{obs}}$ distribution and our best-fit model.

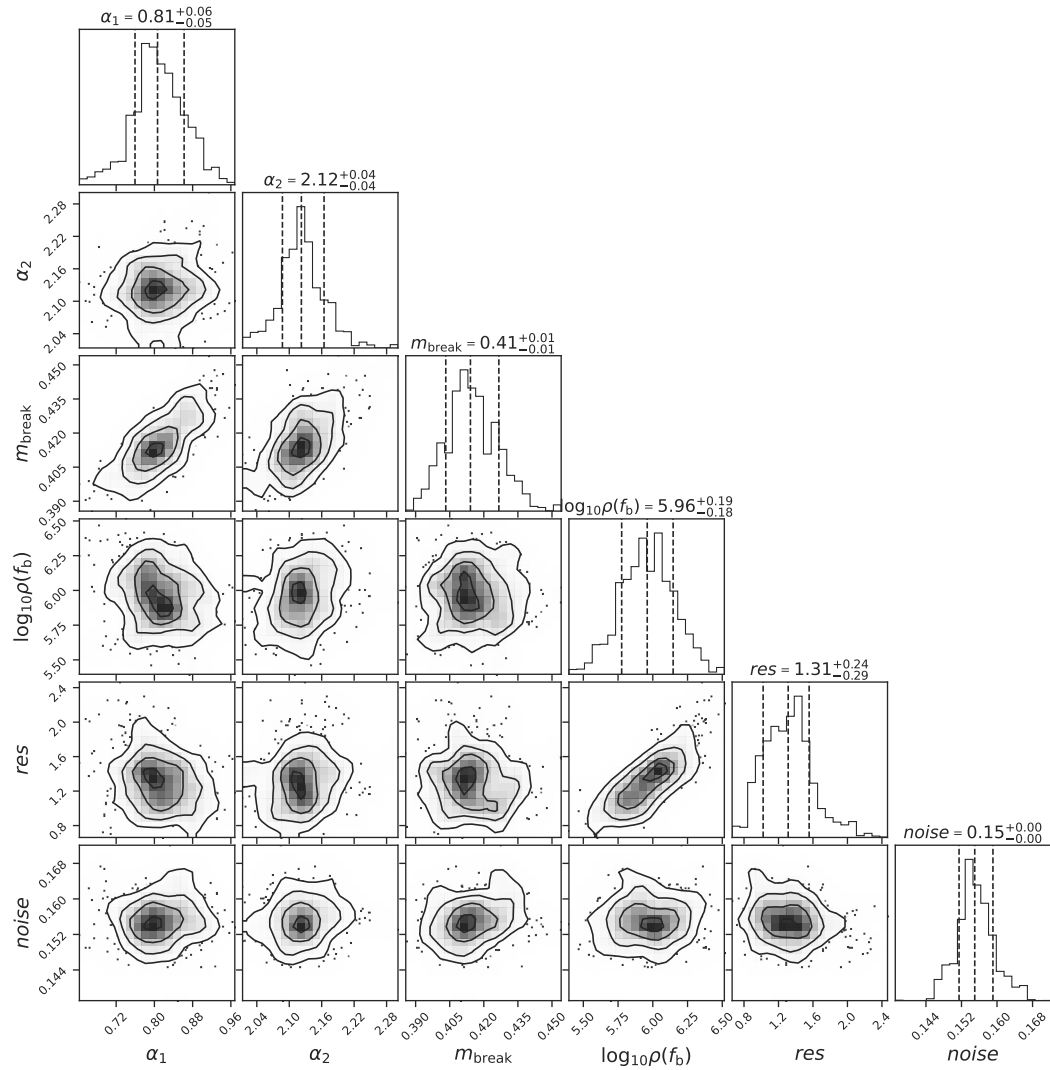


Figure 7. The posterior distribution of the model parameters with our main sample described in Fig. 2.

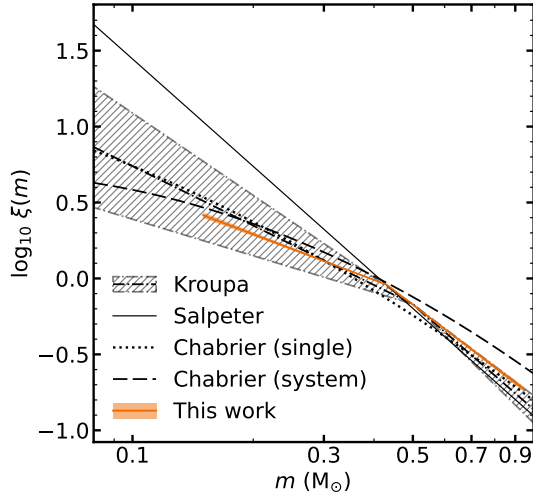


Figure 8. Comparison of the stellar IMF derived from *Gaia* DR3 data and our population synthesis model with canonical IMFs proposed by Salpeter (1955), Kroupa (1992) and Chabrier (2003). The black solid line denotes Salpeter’s IMF with $\alpha = 2.35$. The black dash-dotted line and shaded area describe the Kroupa’s IMF with $\alpha_1 = 1.3 \pm 0.5$ and $\alpha_2 = 2.3 \pm 0.3$. The dotted and dashed lines respectively stand for Chabrier’s IMFs for single stars and systems. The orange dotted line and shaded area defines the IMF derived in this work. Our IMF shows remarkable consistency with Kroupa’s IMF within the 1- σ confidence interval, while exhibiting unprecedented precision.

4 RESULTS

The posterior distribution is plotted in Fig. 7, and the best estimation of the IMF is drawn in Fig. 8 along with all the canonical IMFs. Our best estimation for the averaged field star IMF is $\alpha_1 = 0.81^{+0.06}_{-0.05}$, $\alpha_2 = 2.12^{+0.04}_{-0.04}$ and $m_{\text{break}} = 0.41^{+0.01}_{-0.01}$, which is consistent with the Kroupa IMF but with much smaller uncertainties, owe to the unprecedented number and quality of the *Gaia* data. Compared to Salpeter’s IMF, our IMF (also Kroupa’s and Chabrier’s) are flatter for the mass range $m < 0.41 M_{\odot}$, avoiding the number divergence at the low-mass end. Additionally, the posterior distribution of break point shows slight correlation with α_1 and α_2 respectively.

Our IMF is averaged stellar initial mass function for all the components in the single star and binary systems in the solar neighbourhood field. The evolution of binary orbit evolution is taken considered by the way assuming that stars are born in binaries with the IMF we define and randomly-paired and dynamically evolved based on their binding energy and mass ratio.

The parameter $\log_{10}\rho$ in our model represents the typical density of the characteristic cluster. It will also determine the survived binary fraction and can be compared with the present-day binary fraction in the observational data. The best estimation of $\log_{10}\rho$ is $5.96^{+0.19}_{-0.18}$. Fig. 5 shows the relation between $\log_{10}\rho$ and present-day binary fraction, so our result illustrates that the average binary fraction in the solar neighbourhood is $\sim 25\%$.

The last parameter is the resolution of *Gaia*, and it is calculated as $1.21^{+0.24}_{-0.27}$ arcsec in our model. In the procedure, we distinguish the resolved and unresolved binaries by comparing the angular distance of the systems and this resolution. The resolution will decide the ratio of unresolved systems over all the binary systems, so it has correlation with $\log_{10}\rho$. The official document of *Gaia* has stated that the effective resolution is 1.5 arcsec, at which the number counts

of source pairs as a function of their separation drop below the expected line for a random source distribution for *Gaia* DR3 (Gaia Collaboration et al. 2021a). This value can be affected by the region and source we are observing, and our determination of the resolution of *Gaia* is relatively reasonable, which indicates the reliability of our process.

5 DISCUSSION

5.1 Dynamical evolution operator

First, we will clarify some points about our cluster-mode dynamical evolution operator.

In this operator, we only consider the disruption of binary in the cluster. According to Heggie-Hills law (Heggie 1975; Hills 1975), hard binaries (those with binding energy greater than the average kinetic energy of the stellar cluster) tend to become even “harder” during dynamical evolution, while soft binaries (those with binding energy smaller than the average kinetic energy) become “softer”. As a result, soft binaries eventually tend to undergo dissolution. This paper focuses solely on the process of binary dissolution during dynamical evolution, while other processes such as binary capture, mergers, and coevolution of binary stars have relatively weaker effects (Marks et al. 2011). We also have not considered changes in orbital parameters during the process, as it has been shown by Kroupa & Burkert (2001) that, compared to the broadening of binary separations, dissolution plays the dominant role in dynamical evolution.

Second, why we need the additional part to modulate the mass ratio? We want to modify the mass-ratio distribution from random-pairing shape to today observed shape by a binary disruption process similar to what happens in a cluster’s dynamical evolution. Physically, this process mainly relies on the binding energy of a binary system, and this is exactly how Marks et al. (2011) built their empirical function for cluster’s dynamical evolution. But this physical process is proved to have insignificant influence on the mass-ratio distribution according to Marks et al. (2011) and also our test in Fig. 9. Though in the functional expression of binding energy in Eq. 10, the mass ratio is one of the variables, we can see in the plane of binary period and mass ratio in Fig. 9, where the colour depicts the value of binding energy, that change in mass-ratio hardly affects the value of binding energy. Thus, a process acting on the binding energy can barely modify the mass-ratio distribution.

Besides, in our Bayesian inference, we find that the power-law indices of mass-ratio distribution in our model cannot be well-constrained by the data. The information of the mass-ratio distribution hides in the binary sequence for a simple stellar population (similar chemical composition). However, the stars in the solar neighbourhood have mixed metallicity from $[M/H] = -1.0$ to 0.5 dex, and this mixture wipes out the information of the mass-ratio distribution. It is more likely that we can constrain the distribution when we obtain the metallicity measurement for each star and split them into narrow metallicity bins (e.g., Liu 2019).

5.2 Solutions in different distance bins

In this section, we apply our model on the 0-20 pc, 20-40 pc, 40-60 pc and 80-100 pc subsamples, respectively. If the stellar population is sufficiently mixed in the 100-pc solar neighbourhood, our model

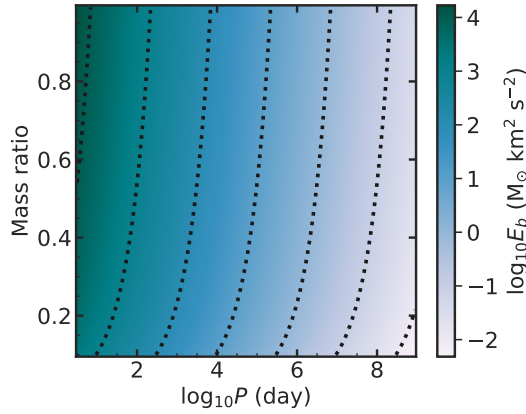


Figure 9. The influence of period and mass ratio on the binding energy according to Kepler’s Third Law. We fix the mass of the primary star to $1.0 M_{\odot}$ in this plot to demonstrate how the binding energy varies with period and mass ratio. The dotted lines depict the contour of the binding energy values. The binding energy mostly relies on the period.

should give invariable IMF parameters and binary fraction. This test will validate the robustness of our model and the uniformity of the stellar population in the solar neighbourhood.

For the first step, we display the effective volume corrected luminosity functions (LF) and ΔM_G distributions for the different distance bins in Fig. 10. We test for the consistency of distributions for each bin with the 80-100 pc LF and ΔM_G distribution. By K-S test, we find that we cannot distinguish the LFs for each subsample with 95% confidence, while each ΔM_G distribution significantly deviates from the 80-100 pc ΔM_G distribution.

According to Kroupa (2001), their nearby LF, ϕ_{near} (from the 5.2-pc volume-limited trigonometric data), and their photometric LF, ϕ_{phot} (from deep photometric pencil-beam observation), differ significantly for stars fainter than $M_V \approx 11.5$ mag. Kroupa (1995b) stated that this discrepancy is not coming from a local over-density of low-mass stars, but from the effect of unresolved multiple systems. Unresolved binary may not substantially affect the faint end of the luminosity function as Kroupa (1995b) claimed. We suspect that the difference in LFs ϕ_{near} and ϕ_{phot} may be due to the combined influence of large statistical uncertainties induced by the small size of dataset in the derivation of ϕ_{near} , Malmquist bias caused by the using of photometric parallax in the derivation of ϕ_{phot} , and effect of unresolved binaries especially for the 5.2-pc volume-limited trigonometric data with its poorer angular resolution respect to *Gaia* DR3.

The unresolved binaries can be more easily detected in ΔM_G distribution. It means that there might be only a small fraction of binary systems that effectively affect the shape of LFs, while the effect of binaries can be more accented in ΔM_G space.

In Fig. 11, we illustrate the derived parameters with our model in different distance bins. The corner plot in Fig. 11 shows 0.5, 1.0, 1.5, 2.0 σ levels of each parameter derived in each distance bin. The uncertainties of each model parameter decline with increasing distance because of the larger volume of data for the farther distance bins. Among these distance bins, all parameters are indistinguishable within the 2-sigma uncertainty level, which shows the robustness of our population synthesis model, and indicates that the stars in the solar neighbourhood are well-mixed. We observe that for stars within 0-20 pc, the parameters α_2 , m_{break} , and $\log_{10} \rho$ are slightly higher than those in other distance bins. The larger values of α_2 and m_{break}

Table 2. The ξ parameter of different IMF measurements.

ξ	Reference
0.6370	Salpeter (1955)
$0.5194^{+0.0581}_{-0.0585}$	Kroupa (1992)
0.4607	Chabrier (2003)
$0.5075^{+0.0112}_{-0.0051}$	This work

are likely due to the effect of saturation in photometric observations, causing *Gaia* to miss a portion of bright stars at such close distances (Gaia Collaboration et al. 2023a). For the same reason, we tend to lose bright unresolved binary sources. Furthermore, given the higher binary fraction for brighter and more massive primary stars, it is reasonable to obtain a lower present-day binary fraction (i.e., higher $\log_{10} \rho$) for the nearby sample.

5.3 Solution for the brighter end

It has been studied that the mean frequency of stellar companions increases from solar-type MS primaries to O-type MS primaries (Moe & Di Stefano 2017). We could expect, if we separate our samples by luminosity into a bright part and a faint part, the binary fraction of the brighter part should be higher than the fainter subsample. We define the brighter part as stars with $M_G \leq 8$ mag, and the posteriors of the model parameters and the fitting result is displayed in Fig. 12 and Fig. 13. The resultant IMF parameters is consistent with the result derived with the whole sample within 2- σ level, while the binary fraction is derived to be higher, which is $\sim 60\%$, compared to our main result. The derived *noise*, which corresponds to the standard deviation of the Gaussian noise added to the simulated ΔM_G distribution, is smaller than our main result. This is reasonable, as the observational uncertainty should be relatively small for brighter stars. This result for the stars at the brighter end once again demonstrates the reliability of our population synthesis model.

5.4 The ξ parameter to compare different IMF measurements

Martín-Navarro et al. (2019) introduces a new quantity, ξ , for an unbiased comparison among different IMF parametrizations. The ξ parameter quantifies the mass fraction locked in low-mass stars, and is defined as

$$\xi \equiv \frac{\int_{0.2}^{0.5} m \cdot X(m) dm}{\int_{0.2}^{1.0} m \cdot X(m) dm}, \quad (20)$$

where $X(m)$ is the IMF expressed in linear mass units.

Martín-Navarro et al. (2019) has calculated that for a Chabrier (2003) IMF, $\xi = 0.4607$; and for Salpeter (1955) IMF, $\xi = 0.6370$. Kroupa (1992) has provided the parameter uncertainty for his IMF, so we can obtain the corresponding $\xi = 0.5194^{+0.0581}_{-0.0585}$. For the IMF derived in this paper, $0.5075^{+0.0112}_{-0.0051}$, with much smaller uncertainty. All ξ values are summarized in Table 2.

6 CONCLUSIONS

In this paper, we remeasure the stellar initial mass function for

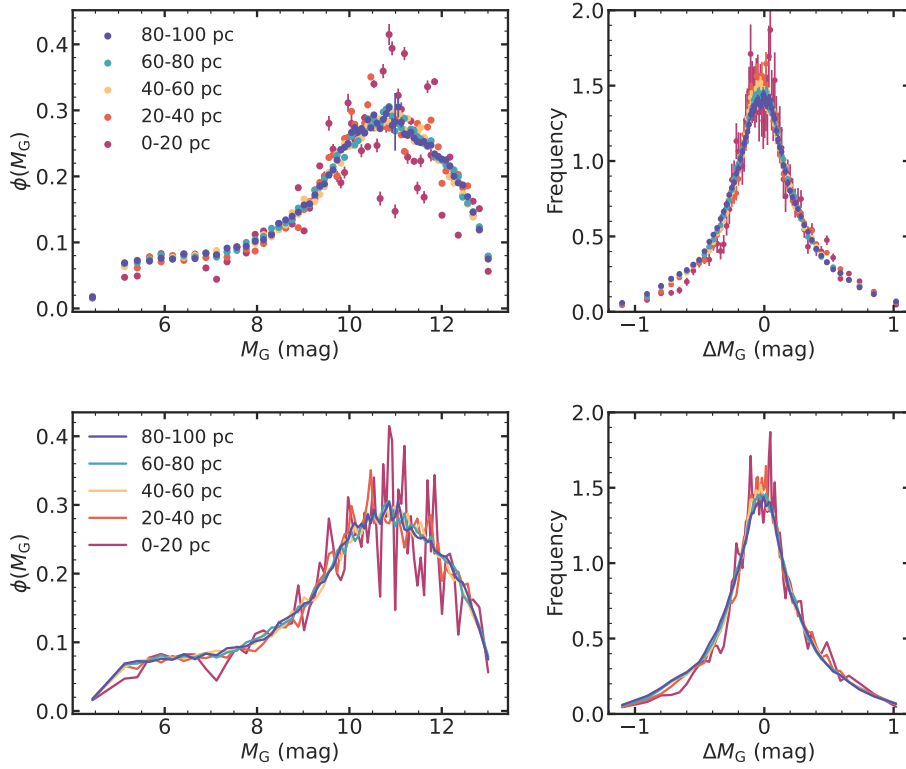


Figure 10. Luminosity functions and ΔM_G distributions for GCNS sample in different distance bins. Top panel: drawn with dots and error bars for each bin. Bottom panel: drawn with lines which facilitates to observe the overall trend.

the field stars in the 100-pc solar neighbourhood in the mass range $0.15 < m/M_\odot < 1.0$. With the up-to-date volume-complete trigonometric parallax data of *Gaia* DR3, this measurement will be the new IMF benchmark for the field stars in the solar neighbourhood. In our forward model for the IMF, we redefine the IMF as the mass distribution with which the stars will form with 100% binarity and be randomly paired at birth, then go through a dynamical evolution similar to a star cluster. And the consequent binary fraction and mass-ratio distribution after the evolution will be used to compare with the observed present-day binary population properties to constrain our model parameters, including α_1 , α_2 , m_{break} (IMF), γ_1 , γ_2 , q_{break} (mass-ratio distribution), res (angular resolution of *Gaia*), and $\log_{10}\rho$ (typical cluster density for the cluster-mode dynamical evolution, related to present-day binary fraction).

Due to the mixture of populations (metallicity and binary properties) of the data, the present-day mass-ratio distribution in our model cannot be well-constrained by the GCNS dataset. Therefore, we fix the parameters of mass-ratio distribution by the information provided by wide binaries compiled by [El-Badry et al. \(2021\)](#). We depict the present-day mass-ratio distribution as a combination of a piece-wise power-law function and an excess of twin binaries, and obtain $\gamma_1 = 1.89^{+0.23}_{-0.20}$, $\gamma_2 = 0.20^{+0.12}_{-0.13}$, $q_{\text{break}} = 0.44^{+0.02}_{-0.02}$, and $F_{\text{twin}} = 0.08^{+0.01}_{-0.01}$. We apply them as Gaussian priors in our Bayesian inference.

Our best estimation for the averaged field star IMF is $\alpha_1 = 0.81^{+0.06}_{-0.05}$, $\alpha_2 = 2.12^{+0.04}_{-0.04}$ and $m_{\text{break}} = 0.41^{+0.01}_{-0.01}$ when apply-

ing the mass-ratio distribution priors above, which is consistent with the Kroupa's and Chabrier's canonical IMFs but with much smaller uncertainties, owe to the unprecedented coverage and quality of the *Gaia* astrometric data. In the meanwhile, our model also give measurement for the binary fraction in the solar neighbourhood. It shows that the density of the characteristic cluster in our model is $\log_{10}\rho = 5.96^{+0.19}_{-0.18}$, which means the fitted present-day binary fraction is $\sim 25\%$. Noted that we only take binary systems into account to get this value. Additionally, we obtain the spatial resolution of *Gaia* DR3 to be $res = 1.31^{+0.24}_{-0.29}$ arcsec, but this value is not so well-constrained and correlated to the cluster density since they collaboratively decide the binary fraction in our model.

In the discussion, we first examine the luminosity functions and ΔM_G distributions for stars in different distance bins 0-20 pc, 20-40 pc, 40-60 pc, 60-80 pc and 80-100 pc. We perform K-S test to check if these luminosity functions and ΔM_G distributions are consistent to each other. The K-S test confirms that luminosity functions for different distance bins cannot be distinguished from each other, and ΔM_G for different distance bins are drawn from different distributions. The outcomes of our K-S test are understandable because: (1) The form of the luminosity function depends on the IMF and mass-luminosity relation. If the stellar population in the 100-pc solar neighbourhood is well-mixed, we should obtain consistent IMFs for different distance bins. (2) The form of the ΔM_G distribution relies mainly on the properties of the binary population, i.e., unresolved binary fraction and present-day mass-ratio distribution. Since it becomes harder for *Gaia*

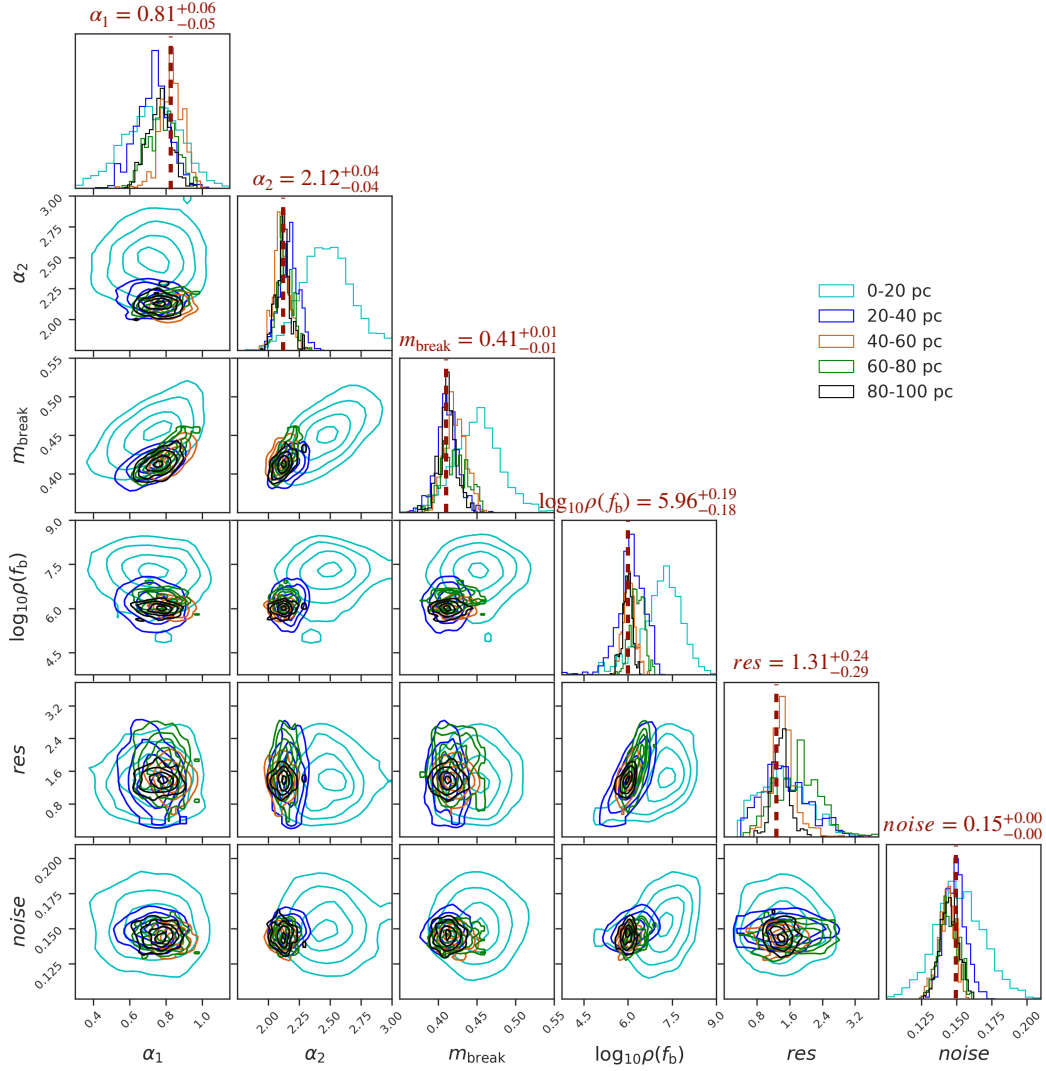


Figure 11. The derived parameter posteriors with our model in different distance bins. The brown vertical dashed lines and titles show the results from the whole 0-100 pc main sample which is demonstrated before in Sec.4 and Fig.7.

to resolve binaries when the distance becomes larger, the proportion of unresolved binaries will increase and cause the variation of the ΔM_G distribution. However, if we consider the angular resolution of *Gaia* in the model, we expect to recover similar overall binary fractions for different distance bins. Our model is then validated giving compatible parameters of IMFs and binary fractions.

We further examine our model by applying it only to the brighter end of the CMD for stellar mass $0.5 < m/M_\odot < 1.0$. Our model is further validated by revealing compatible parameters of IMFs and higher binary fractions for heavier primary stars.

Last, we provide users the ξ parameter for our new IMF facilitating the comparison with measurements on other kinds of populations, which is $\xi = 0.5075^{+0.0112}_{-0.0051}$.

ACKNOWLEDGEMENTS

The authors appreciate discussions with Dan Qiu, Hans-Walter Rix, and Long Wang.

This work used the data from the European Space Agency

(ESA) mission *Gaia* (<https://www.cosmos.esa.int/gaia>), processed by the *Gaia* Data Processing and Analysis Consortium (DPAC; <https://www.cosmos.esa.int/web/gaia/dpac/consortium>). Funding for the DPAC has been provided by national institutions, in particular the institutions participating in the *Gaia* Multilateral Agreement. Guoshoujing Telescope (the Large Sky Area Multi-Object Fiber Spectroscopic Telescope LAMOST) is a National Major Scientific Project built by the Chinese Academy of Sciences. Funding for the project has been provided by the National Development and Reform Commission. LAMOST is operated and managed by the National Astronomical Observatories, Chinese Academy of Sciences.

Facilities: *Gaia*, LAMOST.

Software: IPython (Pérez & Granger 2007), jupyter (Kluyver et al. 2016), pandas (pandas development team 2020), Astropy (Astropy Collaboration et al. 2022), numpy (Harris et al. 2020), scipy (Virtanen et al. 2020), matplotlib (Hunter 2007), PyTorch (Paszke et al. 2017), emcee (Foreman-Mackey et al. 2013a).

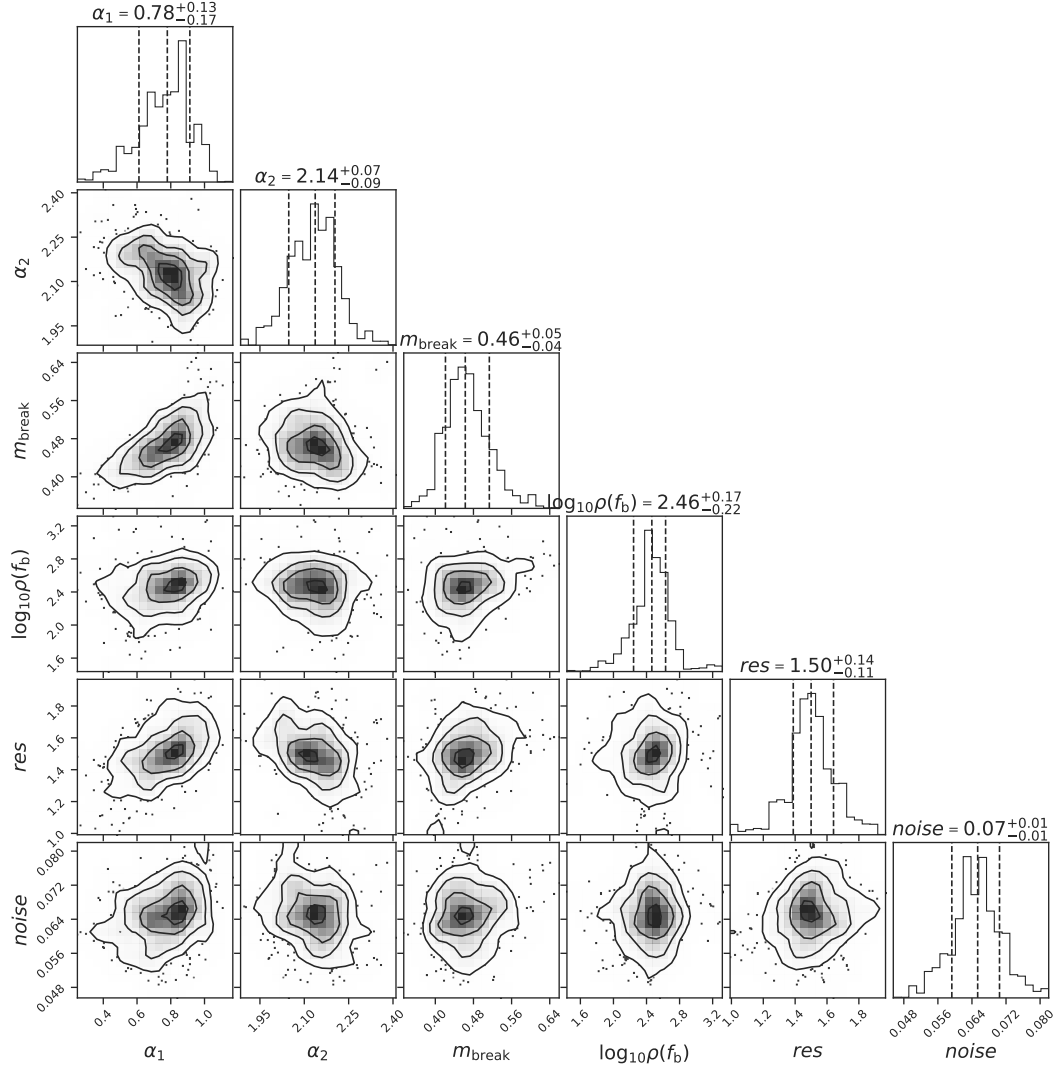


Figure 12. The posterior distribution of the model parameters for stars with $M_G \leq 8$ mag. The best estimation of $\log_{10}\rho = 2.46$ is equivalent to a present-day binary fraction of $\sim 60\%$.

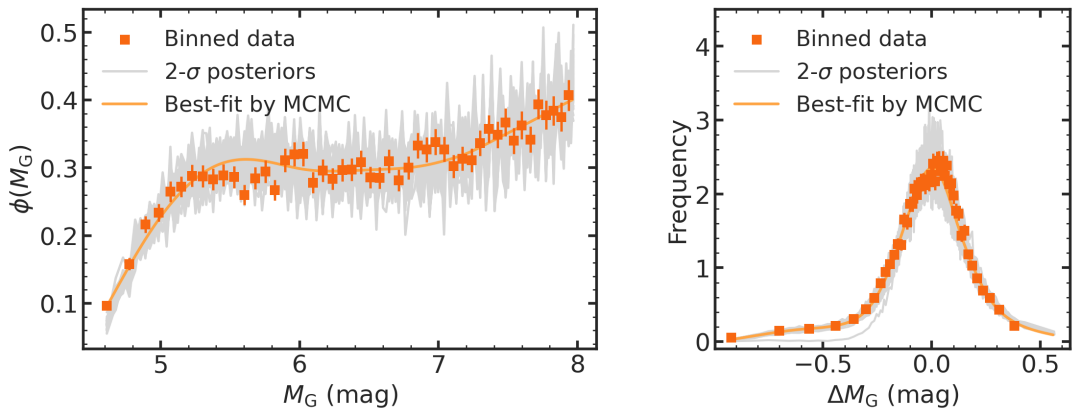


Figure 13. Comparison between observed luminosity function $\phi_{\text{obs}}^{\text{bright}}(M_G)$, $\Delta M_{G,\text{obs}}^{\text{bright}}$ distribution and our best-fit model.

DATA AVAILABILITY

The data underlying this article are available online. The datasets were derived from sources in the public domain: The Gaia Data Archive <https://gea.esac.esa.int/archive/>, and National Astronomical Data Center <https://nadc.china-vo.org/res/r101265/>.

References

- Astropy Collaboration et al., 2022, *ApJ*, 935, 167
- Bailer-Jones C. A. L., Rybizki J., Fouesneau M., Mantelet G., Andrae R., 2018, *AJ*, 156, 58
- Bastian N., de Mink S. E., 2009, *MNRAS*, 398, L11
- Bastian N., Covey K. R., Meyer M. R., 2010, *ARA&A*, 48, 339
- Bochanski J. J., Hawley S. L., Covey K. R., West A. A., Reid I. N., Golimowski D. A., Ivezić Ž., 2010, *AJ*, 139, 2679
- Bonnell I. A., Clarke C. J., Bate M. R., 2006, *MNRAS*, 368, 1296
- Bressan A., Marigo P., Girardi L., Salasnich B., Dal Cero C., Rubele S., Nanni A., 2012, *MNRAS*, 427, 127
- Cantat-Gaudin T., et al., 2023, *A&A*, 669, A55
- Chabrier G., 2003, *ApJ*, 586, L133
- Chen Y., Girardi L., Bressan A., Marigo P., Barbieri M., Kong X., 2014, *MNRAS*, 444, 2525
- Chen Y., Bressan A., Girardi L., Marigo P., Kong X., Lanza A., 2015, *MNRAS*, 452, 1068
- Clark P. C., Glover S. C. O., Klessen R. S., Bromm V., 2011, *ApJ*, 727, 110
- Covey K. R., et al., 2008, *AJ*, 136, 1778
- Duchêne G., Kraus A., 2013, *ARA&A*, 51, 269
- Edenhofer G., Zucker C., Frank P., Saydjari A. K., Speagle J. S., Finkbeiner D., Enßlin T. A., 2024, *A&A*, 685, A82
- El-Badry K., Rix H.-W., Tian H., Duchêne G., Moe M., 2019, *MNRAS*, 489, 5822
- El-Badry K., Rix H.-W., Heintz T. M., 2021, *MNRAS*, 506, 2269
- Felten J. E., 1976, *ApJ*, 207, 700
- Foreman-Mackey D., et al., 2013a, emcee: The MCMC Hammer, *Astrophysics Source Code Library*, record ascl:1303.002
- Foreman-Mackey D., Hogg D. W., Lang D., Goodman J., 2013b, *PASP*, 125, 306
- Gaia Collaboration et al., 2018, *A&A*, 616, A1
- Gaia Collaboration et al., 2021a, *A&A*, 649, A1
- Gaia Collaboration et al., 2021b, *A&A*, 649, A6
- Gaia Collaboration et al., 2023a, *A&A*, 674, A1
- Gaia Collaboration et al., 2023b, *A&A*, 674, A34
- Golovin A., Reffert S., Just A., Jordan S., Vani A., Jahreiß H., 2023, *A&A*, 670, A19
- Gould A., Bahcall J. N., Flynn C., 1996, *ApJ*, 465, 759
- Griv E., Gedalin M., Pietrukowicz P., Majaess D., Jiang I.-G., 2021, *MNRAS*, 502, 4194
- Guszejnov D., Krumholz M. R., Hopkins P. F., 2016, *MNRAS*, 458, 673
- Hallakoun N., Maoz D., 2021, *MNRAS*, 507, 398
- Harris C. R., et al., 2020, *Nature*, 585, 357
- Heggie D. C., 1975, *MNRAS*, 173, 729
- Hills J. G., 1975, *AJ*, 80, 809
- Hunter J. D., 2007, *Computing in Science & Engineering*, 9, 90
- Jahreiß H., Wielen R., 1997, in Bonnet R. M., et al., eds, *ESA Special Publication Vol. 402, Hipparcos - Venice 1997*. pp 675–680
- Johnson N. L., 1949, *Biometrika*, 36, 149
- Kluyver T., et al., 2016, in , IOS Press. pp 87–90, doi:10.3233/978-1-61499-649-1-87
- Kroupa P., 1992, PhD thesis, University of Cambridge, UK
- Kroupa P., 1995a, *MNRAS*, 277, 1507
- Kroupa P., 1995b, *ApJ*, 453, 358
- Kroupa P., 2001, *MNRAS*, 322, 231
- Kroupa P., Burkert A., 2001, *ApJ*, 555, 945
- Kroupa P., Weidner C., Pflamm-Altenburg J., Thies I., Dabringhausen J., Marks M., Maschberger T., 2013, *The Stellar and Sub-Stellar Initial Mass Function of Simple and Composite Populations*. Springer Netherlands, p. 115–242, doi:10.1007/978-94-007-5612-0_4, http://dx.doi.org/10.1007/978-94-007-5612-0_4
- Kroupa P., Gjerger E., Jerabkova T., Yan Z., 2024, *The initial mass function of stars*, <https://arxiv.org/abs/2410.07311>
- Li J., Liu C., Zhang Z.-Y., Tian H., Fu X., Li J., Yan Z.-Q., 2023, *Nature*, 613, 460
- Lindgren L., et al., 2021, *A&A*, 649, A4
- Liu C., 2019, *MNRAS*, 490, 550
- Liu C., et al., 2017, *Research in Astronomy and Astrophysics*, 17, 096
- Lutz T. E., Kelker D. H., 1973, *PASP*, 85, 573
- Maíz Apellániz J., Úbeda L., 2005, *ApJ*, 629, 873
- Marigo P., et al., 2017, *ApJ*, 835, 77
- Marks M., Kroupa P., Oh S., 2011, *MNRAS*, 417, 1684
- Martín-Navarro I., et al., 2019, *A&A*, 626, A124
- Miller G. E., Scalo J. M., 1979, *ApJS*, 41, 513
- Moe M., Di Stefano R., 2017, *ApJS*, 230, 15
- Niu Z., Yuan H., Liu J., 2023, *ApJ*, 950, 104
- Parker R. J., Reggiani M. M., 2013, *MNRAS*, 432, 2378
- Pastorelli G., et al., 2019, *MNRAS*, 485, 5666
- Pastorelli G., et al., 2020, *MNRAS*, 498, 3283
- Paszke A., et al., 2017, in *NIPS-W*.
- Penoyre Z., Belokurov V., Evans N. W., 2022, *MNRAS*, 513, 5270
- Pérez F., Granger B. E., 2007, *Computing in Science and Engineering*, 9, 21
- Qiu D., Li J., Zhang B., Liu C., Tian H., Niu Z., 2024, *MNRAS*, 527, 11866
- Raghavan D., et al., 2010, *ApJS*, 190, 1
- Reid I. N., Gizis J. E., Hawley S. L., 2002a, *AJ*, 124, 2721
- Reid I. N., Gizis J. E., Hawley S. L., 2002b, *AJ*, 124, 2721
- Riello M., et al., 2021, *A&A*, 649, A3
- Salpeter E. E., 1955, *ApJ*, 121, 161
- Scalo J. M., 1986, *Fundamentals Cosmic Phys.*, 11, 1
- Schmidt M., 1968, *ApJ*, 151, 393
- Skrutskie M. F., et al., 2006, *AJ*, 131, 1163
- Sollima A., 2019, *MNRAS*, 489, 2377
- Tang J., Bressan A., Rosenfield P., Slemmer A., Marigo P., Girardi L., Bianchi L., 2014, *MNRAS*, 445, 4287
- Tinney C. G., Reid I. N., Mould J. R., 1993, *ApJ*, 414, 254
- Vazdekis A., et al., 2015, *MNRAS*, 449, 1177
- Virtanen P., et al., 2020, *Nature Methods*, 17, 261
- Vogel M., 2017, *Contemporary Physics*, 58, 193
- Wang L., Iwasawa M., Nitadori K., Makino J., 2020, *MNRAS*, 497, 536
- Weidner C., Kroupa P., 2005, *ApJ*, 625, 754
- York D. G., et al., 2000a, *AJ*, 120, 1579
- York D. G., et al., 2000b, *AJ*, 120, 1579
- pandas development team T., 2020, pandas-dev/pandas: Pandas, doi:10.5281/zenodo.3509134, <https://doi.org/10.5281/zenodo.3509134>

APPENDIX A: EFFECTIVE VOLUME OF GCNS

In this appendix, we describe our approach to testing the completeness of the GCNS catalog. Since the selection function shows minimal variation with colour $G_{BP} - G_{RP}$ (Reid et al. 2002b), we apply the classical V_{\max} analysis (Schmidt 1968; Felten 1976; Tinney et al. 1993) to our data using the absolute magnitude M_G . In the V_{\max} method, the parameter d_{\max} represents the maximum distance at which a star of a given magnitude M_G can be detected. Using this distance and the solid angle subtended by our data sample, we calculate the “maximum volume” for each star—the largest volume of space within which this star remains detectable. The sum of the inverse of these V_{\max} values provides an unbiased estimate of the stellar density $\phi(M_G)dM_G$. This method eliminates the need to partition the sample into smaller volumes to ensure completeness for fainter objects. Instead, it allows the distance limit of our effectively “volume-limited” sample to vary as a function of luminosity, thereby

maximizing the statistical power of our analysis while maintaining proper completeness corrections.

Following Tinney et al. (1993), if considering arbitrary density profile of the stars, we can define a generalized volume for a star within a distance d ,

$$V_{\text{gen}} = \Omega \int_0^d \frac{r^2 \rho dr}{\rho_0}, \quad (\text{A1})$$

where Ω is the solid angle covered by the data, ρ_0 is the local space density at the position of the sun, and r is the stellar distance.

Thus, the maximum generalized volume (also the “effective volume”) will be

$$V_a = \Omega \int_0^{d_{\text{max}}} \frac{r^2 \rho dr}{\rho_0}, \quad (\text{A2})$$

and the unbiased estimator for $\phi(M_G)$ will be

$$\phi(M_G) = \sum \frac{1}{V_a} \quad (\text{A3})$$

And the next question should be the value of d_{max} for different M_G . For regular quality cuts on a catalog, the maximum distance can be set by three different aspects, the cut on parallax ϖ^{lim} , the cut on the apparent magnitude G^{lim} , and the cut on the signal-to-noise ratio of parallax $(\sigma_{\varpi}/\varpi)^{\text{lim}}$, according to the work Reid et al. (2002b). Under the assumption of isotopic, homogeneous stellar density profile, and of no extinction condition, the derived effective volume after these three cuts will be similar to Fig.6 in Reid et al. (2002b) for different M_G .

However, the catalog GCNS applied a machine-learning way to collect stars with reliable astrometry and with non-zero probability to be in the 100-pc volume. The cuts can then be rather vague and hard to express in an analytical way. Therefore, we conduct the Kolmogorov–Smirnov (K-S) test to determine if our data is drawn from the same density distribution as synthetic sources generated with a exponential distribution $n(R_{xy}, z)$ relative to the Galactic center. We operate the K-S test comparing the stellar density distribution along the distance from the sun $n(d)$ for observed data and synthetic sources in sliding bins of M_G with 0.1 mag step and 1 mag bin width, favouring robustness and resolution in the meanwhile. In an individual M_G bin, the test is done in different distance ranges, and this can give us the maximal distance in the M_G bin where the data remain the same distribution as the synthesized one. Fig.A1 illustrates the P-value from the K-S test versus the distance in pc for the M_G bin 12-13 mag. We adopt the P-value threshold of 0.001 to reject the null hypothesis, so in this M_G bin, stars are in the same density profile as the synthesized one up to the distance 100 pc, which means that the data are volume completed up to 100 pc.

APPENDIX B: METALLICITY DISTRIBUTION IN THE SOLAR NEIGHBOURHOOD

In this section, we discuss how we extract the intrinsic metallicity distribution (MDF) in the solar neighbourhood that will be treated as a sampling function for the metallicity of our simulated stars. We make use of the metallicity measurement derived from the Data Release Nine (DR9) of LAMOST Low-Resolution Spectroscopic

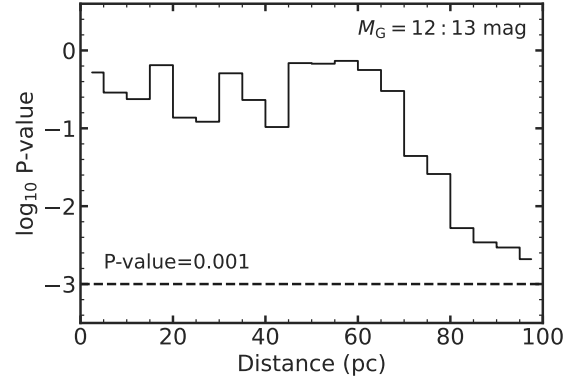


Figure A1. P-value from the K-S test versus distance in pc for the M_G bin 12-13 mag.

Survey (LRS)¹. For A-, F-, G-, and K-type stars, we download the LAMOST LRS Stellar Parameter Catalog of A, F, G, and K Stars from the official website and use the metallicity provided in the catalog. Niu et al. (2023) investigated the systematic errors of stellar chemical abundances in the LAMOST and Gaia databases. We use the correction function in Niu’s paper to calibrate the LAMOST DR9 metallicity for A, F, G, K stars. The metallicity measurement for M-type stars is a more complicated problem, for their faint nature and our relatively poor understanding of their atmospheric model (Qiu et al. 2024). Qiu et al. (2024) empirically calibrate the LAMOST DR9 metallicity of M-type stars using wide binaries with a F-, G-, or K-dwarf primary and a M-dwarf companion, taking the systematic calibration in Niu et al. (2023) into consideration. Since what we desire is an averaged MDF covering stars from $M_G = 4$ mag to $M_G = 12.1$ mag, we combine the LAMOST official AFGK-star catalog with metallicity corrected ourselves and the M-type star catalog provided by Qiu et al. (2024) to perform the calculation.

In order to eliminate selection effects that might act on the two catalogs, we refer to the method in Liu et al. (2017), which recovered the selection function by comparing the distribution of the spectroscopic stars (here referred to as our LAMOST catalogs) with that of the photometric dataset (here referred to as *Gaia* DR3) in a 4-dimensional space of colour, apparent magnitude, and 2-D position. The selection function $S(c, m, l, b)$ is defined as

$$S(c, m, l, b) = \frac{n_{\text{sp}}(c, m, l, b)}{n_{\text{ph}}(c, m, l, b)}, \quad (\text{B1})$$

where c, m, l, b are respectively colour, apparent magnitude, Galactic longitude, and Galactic latitude. $n_{\text{sp}}(c, m, l, b)$ is the stellar density of the spectroscopic survey, and $n_{\text{ph}}(c, m, l, b)$ the stellar density of the spectroscopic survey at certain point of this 4-dimensional space. In order to improve the precision of the computation, Liu et al. (2017) calculate $S^{-1}(c, m, l, b)$ instead of S in their paper. Before we apply their procedure, we acquire the interstellar extinction from Edenhofer et al. (2024) and compute the intrinsic absolute magnitude $M_{G,0}$ with the geographical distance r_{geo} estimated by Bailer-Jones et al. (2018) for stars in both catalogs. Then we cut our FGK-dwarf samples with $4.0 < M_{G,0} < 7.6$ mag and $100 < r_{\text{geo}} < 300$ pc, and cut the M-dwarf catalog with $8.5 < M_{G,0} < 12.1$ mag and $20 < r_{\text{geo}} < 160$ pc, to guarantee both the coverage of our interested

¹ <http://www.lamost.org/dr9/v2.0/>

stellar mass range and sample completeness. Then we perform Liu's program in equal-frequency bins of metallicity to avoid the bias caused by uneven relative Poisson error (Maíz Apellániz & Úbeda 2005). Fig.B1 demonstrates how the value $S^{-1}(c, m, l, b)$ varies with metallicity and absolute magnitude for FGK-dwarfs and M-dwarfs, respectively. We treat $S^{-1}(c, m, l, b)$ as counting weights of each star to correct for the selection effect of our LAMOST DR9 catalogs.

We resample our data with $S^{-1}(c, m, l, b)$ (normalised to 0-1) as the possibility. In this way, stars suffered from severer selection effect will be more likely to be retained. Then, since the metallicity of FGK-dwarfs possess smaller measurement uncertainty compared to that of the M-dwarfs, we should first extract the intrinsic metallicity distributions of both kinds of samples. We choose the Johnson's SU distribution to fit for the intrinsic metallicity distributions. The Johnson's SU-distribution is a four-parameter probability distribution first investigated by N. L. Johnson in 1949 (Johnson 1949). It is a transformation of the normal distribution which can be easily sampled from:

$$Y = \gamma + \delta \sinh^{-1} \left(\frac{X - \text{loc}}{\text{scale}} \right) \quad (\text{B2})$$

where $Y \sim \mathcal{N}(0, 1)$, and X is the random variable that is Johnson's SU distributed. Considering this Johnson's SU intrinsic form coupled with an observational model perturbed by noise, the likelihood for each data point can be formalized as:

$$p(z_{\text{obs},i} | \sigma_{z,i}^2, \gamma, \delta, \text{loc}, \text{scale}) = \int_{z_{\text{min}}}^{z_{\text{max}}} \mathcal{N}(z_{\text{obs},i} | z, \sigma_{z,i}^2) p_{\text{intrinsic}}(z | \gamma, \delta, \text{loc}, \text{scale}) dz. \quad (\text{B3})$$

The joint likelihood should be:

$$\mathcal{L} = \prod_i p(z_{\text{obs},i} | \sigma_{z,i}^2, \gamma, \delta, \text{loc}, \text{scale}), \quad (\text{B4})$$

where we use z to stand for the intrinsic metallicity of each star, and z_{obs} as the observational metallicity in our catalogs which is perturbed by observational uncertainty $\sigma_{z,i}$.

The best-fit parameters for our MDFs are $\gamma = 1.14^{+0.22}_{-0.16}$, $\delta = 1.74^{+0.15}_{-0.09}$, $\text{loc} = 0.22^{+0.04}_{-0.03}$, $\text{scale} = 0.28^{+0.02}_{-0.02}$ for FGK-type stars, and $\gamma = 0.47^{+0.18}_{-0.34}$, $\delta = 1.68^{+0.37}_{-0.25}$, $\text{loc} = 0.09^{+0.03}_{-0.05}$, $\text{scale} = 0.20^{+0.06}_{-0.04}$ for M-type stars. We plot our fitting results in Fig.B2.

In order to obtain the overall metallicity distribution for stars in the M_G range from 4 to 12.1 mag, we conduct a weighted average between the intrinsic MDFs of FGK-stars and M-stars. The weights should be their respective numbers of selection-function-resampled objects in the same distance range, which is about 1 versus 2.6 for our FGK- and M-dwarf samples in their overlapped distance of 100-160 pc. Thus, the parameters that we apply to depict the intrinsic metallicity distribution function in the solar neighbourhood are $\gamma = 0.46$, $\delta = 1.48$, $\text{loc} = 0.09$, $\text{scale} = 0.20$.

APPENDIX C: MEASUREMENT FOR THE PRESENT-DAY MASS-RATIO DISTRIBUTION IN THE SOLAR-NEIGHBOURHOOD WITH WIDE BINARIES

As stated before, we could not constrain the mass-ratio distribution with GCNS since it is a mixture of different stellar population and the information for mass-ratio distribution might be wiped out.

Therefore, we fix the present-day mass-ratio distribution with some reasonable parameter value in our model. We use the wide binary catalog published by El-Badry et al. (2021) to derive the present-day mass-ratio distribution. Selection effect should be clearly considered during this derivation. The completeness for wide binaries with narrower separations decreases more significantly when the distance goes up, so we should balance between the farthest distance for the sample and the number of sample to assure wider range of separation we cover and the significance for the signal. We make following cuts:

(1) If we adopt the *Gaia* angular resolution with 1.5 arcsec as stated in Gaia Collaboration et al. (2021a), we can guarantee that wide binaries with projected angular resolution larger than 100 AU can be resolved if we restrain the distance to be smaller than 60 pc. So the cuts will be $\varpi \leq 16.7$ mas and $\text{sep_AU} > 100$ AU.

(2) To reduce the occurrence of chance alignment, we make the cut with the parameter given by El-Badry et al. (2021), $R_{\text{chance_align}} \leq 0.75$, which is the value removing most chance alignments according to their investigation. Since we restrict the distance to a small volume, this relatively loose cut on $R_{\text{chance_align}}$ is sufficient. This cut will remove about 1% of our sources.

At last we obtain $\sim 2,100$ pairs of wide binaries. We use the PARSEC model version 1.2s to transform brightness and colour to mass and metallicity, which is demonstrated in Fig.C1, and then we can obtain the mass-ratio distribution in Fig.C2. We parametrize this distribution following Moe & Di Stefano (2017), which includes a broken power-law to describe the distribution at $0.2 < q < 0.95$ with power-law indices γ_1 and γ_2 , and the break point q_{break} , and includes the twin binary fraction F_{twin} . The best-fitting result is displayed in Fig.C3 with $\gamma_1 = 1.89^{+0.23}_{-0.20}$, $\gamma_2 = 0.20^{+0.12}_{-0.13}$, $q_{\text{break}} = 0.44^{+0.02}_{-0.02}$, $F_{\text{twin}} = 0.08^{+0.01}_{-0.01}$, and $C = 0.93^{+0.02}_{-0.02}$ which is a normalization parameter for the mass-ratio probability function.

We should notice that in practice we use this distribution to represent the mass-ratio distribution for the unresolved binaries in the solar neighbourhood. So here we make a strong assumption that the mass-ratio distribution for binaries with separation wider than 100 AU is representative for all binaries.

This paper has been typeset from a \LaTeX file prepared by the author.

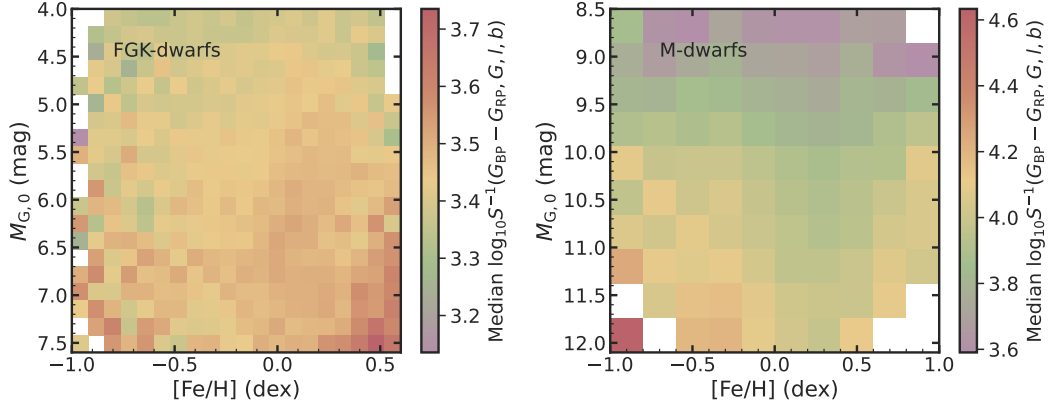


Figure B1. The distribution of inverted selection functions $\log_{10} S^{-1}(G_{\text{BP}} - G_{\text{RP}}, G, l, b)$ of LAMOST DR9 AFGK-type and M-type catalogs.

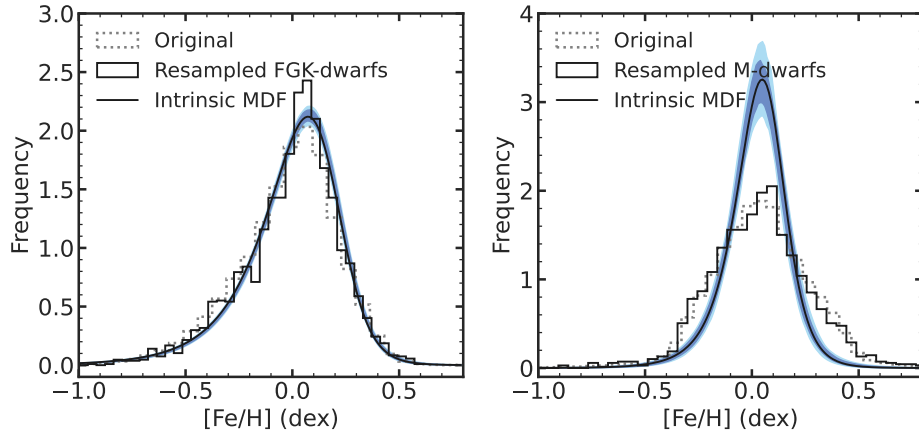


Figure B2. Original and resampled FGK- and M-dwarf's metallicity distributions. one- and two-sigma posteriors of the intrinsic metallicity distributions are drawn with deep blue and light blue shaded areas. The best fit Johnson's SU functions of the intrinsic metallicity distributions are plotted with solid black lines in both plots.

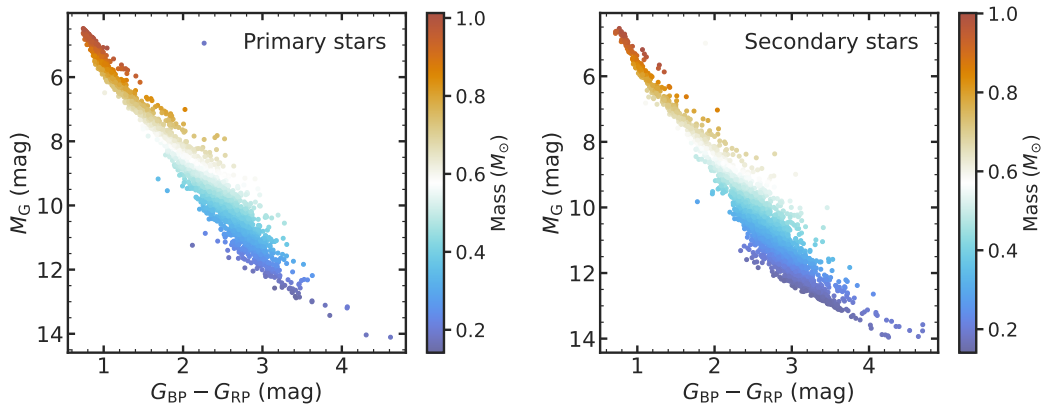


Figure C1. Masses obtained by interpolation of PARSEC isochrones of primary and secondary stars for wide binary systems with $\varpi \leq 16.7$ mas and $\text{sep} > 100$ AU from [El-Badry et al. \(2021\)](#)'s catalog.

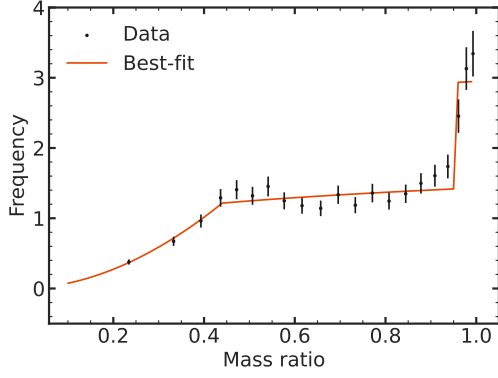


Figure C2. Mass-ratio distribution for wide binary systems with $\varpi \leq 16.7$ mas and $\text{sep} > 100$ AU. The red solid line shows our best fitting result with $\gamma_1 = 1.89^{+0.23}_{-0.20}$, $\gamma_2 = 0.20^{+0.12}_{-0.13}$, $q_{\text{break}} = 0.44^{+0.02}_{-0.02}$, $F_{\text{twin}} = 0.08^{+0.01}_{-0.01}$, and $C = 0.93^{+0.02}_{-0.02}$.

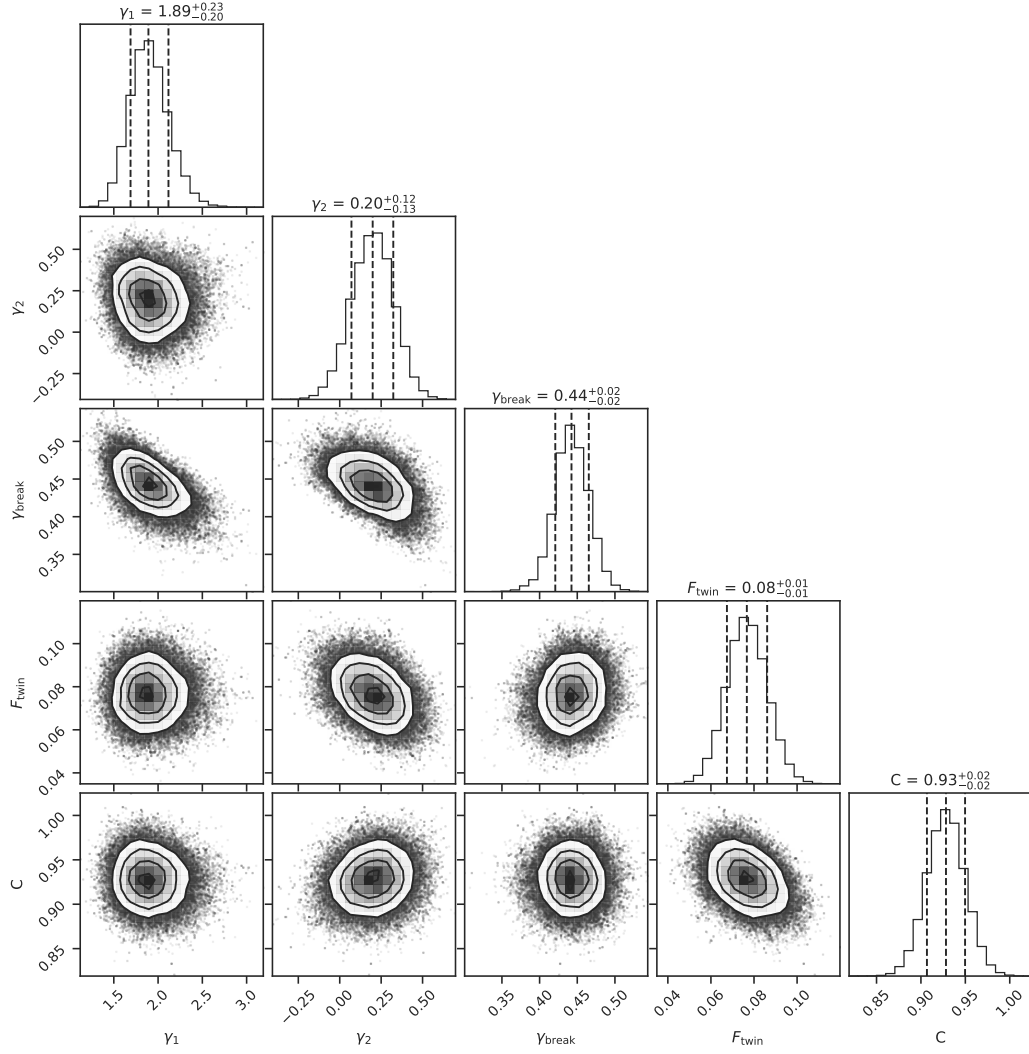


Figure C3. Posterior distribution for the parameters modeling the wide binary mass-ratio distribution.